communications biology

A Nature Portfolio journal

Article

https://doi.org/10.1038/s42003-025-08484-z

Tissue-engineered neuromuscular organoids

Beatrice Auletta[1,2,3], Pietro Chiolerio[1,2], Giada Cecconi[1,2], Lucia Rossi[1,2], Luigi Sartore[1,2], Francesca Cecchinato[1,2], Gilda Barbato[2], Agnese Lauroja[2], Edoardo Maghin[4], Maria Easler[2], Paolo Raffa[2], Silvia Angiolillo[3,5], Wei Qin[3,5], Roberta Frison[3,5], Sonia Calabrò[1], Chiara Villa[6], Onelia Gagliano[3,5], Cecilia Laterza[3,5], Davide Cacchiarelli[7,8,9], Matilde Cescon[1], Monica Giomo[3], Yvan Torrente[6,10], Camilla Luni[11], Martina Piccoli[4], Nicola Elvassore[3,5] & Anna Urciuolo[1,2] ✉

Skeletal muscle development, homeostasis, and function rely on complex interactions among multiple cell types and the extracellular matrix (ECM). Developing in vitro models that recapitulate both intrinsic cellular and extrinsic ECM elements of innervated skeletal muscle is crucial for advancing basic biology and disease modeling studies. Here, we combine tissue engineering approaches with human induced pluripotent stem cell (hiPSC) technology to create tissue-engineered neuromuscular organoids (t-NMOs). Using decellularized muscles as scaffolds, hiPSCs differentiate to form organoids that establish a continuum with the provided biomaterial. After 30 days, t-NMOs exhibit compartmentalized neural and muscular components that establish functional interactions, allowing muscle contraction. We demonstrate the model's potential by creating Duchenne Muscular Dystrophy patient-specific t-NMOs, that recapitulate the reduced skeletal muscle contraction and altered calcium dynamics typical of the disease. Altogether, our study presents a tissue-engineered organoid that model the human neuromuscular system (dys)function, highlighting the potential of applying the ECM in organoid engineering.

Achievements in stem cell technology have opened new frontiers to increase our knowledge on the human neuromuscular system development and biology, and to produce in vitro tools applicable for modeling neuromuscular disorders and for preclinical studies[1–8]. In particular, hiPSCs have been recently used to derive organoids that contain isogenic and multiple cell types of key importance for the human neuromuscular system[1,3,5,7,8]. Indeed, the generation of a functional neuromuscular system requires a complex and coordinated communication between the contractile cells of the tissue, the myofibers, and the motor neuron (MN) axon terminals at the level of the NMJ[6,9,10]. This cellular communication, together with the action of other resident cell types, creates a circuit of cross-trophism that guarantees neuromuscular system development[2,11–13], maturation[11], and maintenance[14]. Aside from intrinsic cellular elements, such biological processes also require the intervention of an extrinsic element, the 3D environment provided by the ECM, which has tissue-specific properties[13,15,16].

However, the skeletal muscle ECM has never been provided as an extrinsic element to hiPSCs during organoid development. Previous studies showed that during development, ECM components guide myogenic commitment and differentiation[17,18], neuronal axon pathfinding[19], and NMJ formation[12–14]. Moreover, in the adult skeletal muscle, a specialized ECM network surrounds each myofiber, enwraps parallel myofiber bundles and finally allows the assembly of an entire muscle[17,18]. This 3D organization of the ECM is essential for muscles to contract as a functional syncytium and to generate force[20]. The ECM also accommodates and sustains stem and supporting cells[21–23]. On the same line, peripheral nerves are packed by the ECM to form parallel axon bundles that depart from the spinal cord[24–26] to

[1]Department of Molecular Medicine, University of Padova, Padova, Italy. [2]Neuromuscular Engineering lab, Istituto di Ricerca Pediatrica, Città della Speranza, Padova, Italy. [3]Department of Industrial Engineering, University of Padova, Padova, Italy. [4]Tissue Engineering lab, Istituto di Ricerca Pediatrica, Città della Speranza, Padova, Italy. [5]Veneto Institute of Molecular Medicine, Padova, Italy. [6]Stem Cell Laboratory, Dino Ferrari Center, Department of Pathophysiology and Transplantation, Università di Milano, Milan, Italy. [7]Telethon Institute of Genetics and Medicine (TIGEM), Armenise/Harvard Laboratory of Integrative Genomics, Pozzuoli, Italy. [8]Department of Translational Medicine, University of Naples "Federico II", Naples, Italy. [9]Genomics and Experimental Medicine Program, Scuola Superiore Meridionale, Naples, Italy. [10]Neurology Unit, Fondazione IRCCS Ca' Granda Ospedale Maggiore Policlinico, Milan, Italy. [11]Department of Civil, Chemical, Environmental and Materials Engineering (DICAM), University of Bologna, Via Terracini 28, Bologna, Italy. ✉e-mail: anna.urciuolo@unipd.it

reach the skeletal muscle and build NMJs, where a specialized ECM is present and required for NMJ homeostasis[27,28].

Thus, we hypothesized that the ECM proper of the innervated skeletal muscle could possess environmental imprinting cues able to sustain the derivation of tissue engineered-neuromuscular organoids (t-NMO) from hiPSCs. To test this hypothesis and to provide a 3D environment that could mimic as much as possible the one present in the innervated skeletal muscle to hiPSCs, we implemented decellularized skeletal muscles (dSkMs) in our study. Indeed, dSkMs are derived starting from the native skeletal muscle, which is treated with reagents that allow nuclei removal and preservation of the ECM composition and 3D architecture of the native tissue[29–34]. We and others previously showed that dSkMs can be used as a tissue-engineered scaffold able to guide and improve muscle regeneration in volumetric muscle loss models, promoting new muscle formation from adult stem cells, as well as nervous system integration and NMJ regeneration[29,32,35,36]. Moreover, dSkMs can be recellularized with human adult cells for the derivation of tissue-engineered 3D in vitro models of skeletal muscle[31,35], and also be used in vitro to study the myogenesis of adult muscle stem cells[29,33,37] and fetal neural axon sprouting[38].

Here, we show that hiPSCs seeded onto dSkM and subjected for 30 days to a small-molecule based neuromuscular differentiation protocol invade the dSkM and assemble into a 3D multiscale construct to form functional t-NMOs. In t-NMOs neuronal and muscular components compartmentalize and the neuromuscular system integrates via long neuritic projections that reach bundles of myofibers. To characterize t-NMOs, we combined morphometric, RNA sequencing and functional analyses. Thirty days after hiPSC differentiation t-NMOs show not only differentiated myofibers and neurons, but also skeletal muscle and neural stem cells, as well as muscular and neuronal supporting cell types. Moreover, at this stage of differentiation t-NMOs also display elements of the NMJ and functional neuromuscular connection. Overall, we found that dSkM improves the maturity of the neuromuscular system in vitro model.

Finally, we show that t-NMOs can be used to mimic in vitro the neuromuscular system of healthy donors and DMD patients. DMD is a neuromuscular disease due to mutations in the dystrophin gene and characterized by a progressive muscle-wasting condition[39]. Dystrophin connects the contractile apparatus inside the myofiber to the ECM, and is enriched at the NMJ[10,11,14]. Here we show that upon neurotransmitter stimulation reduced muscle contraction and calcium dysregulation was observed in DMD t-NMOs, mimicking the cellular phenotype of DMD skeletal muscle[39–42].

Results

DSkMs allow the derivation of tissue-engineered NMOs (t-NMO)

Based on the myogenic and neurotrophic properties exerted by dSkMs on adult stem cells[30,38], here we hypothesized that dSkMs could sustain the production of t-NMOs when provided as 3D scaffold to hiPSCs subjected to small molecule-based differentiation protocol (Fig. 1a). Among different types of muscles, we decided to implement an already well characterized dSkM derived from murine diaphragms[31,32,34,35,37]. In fact, the unique anatomy and homogeneous neuromuscular system spatial distribution of the diaphragm[43,44] allowed us to surgically derive multiple scaffolds from each entire dSkM and to obtain microscopic-friendly scaffolds for monitoring cell culture. It was previously shown that the dSkMs used in this study preserve structural and topographical features of native tissue[31,32,34]. Here we also confirmed that the dSkMs preserved the mechanical properties of freshly isolated diaphragms, as shown by the measurement of Young's modulus via atomic force microscopy (Fig. 1b).

Thus, hiPSCs were seeded as single cells onto dSkMs and after two days of cell culture directly differentiated adapting a widely used differentiation protocol, which is based on small molecules and growth factors administration to recapitulate the early embryonic developmental events that lead to myogenic commitment and later to myogenic terminal differentiation[45]. Notably, such protocol has been shown to promote not only skeletal muscle differentiation, but also to generate other non-muscular cell types in conventional cell culture systems, including neurons and Schwann cells[45–47]. Thus, from now on, we will refer to this as neuromuscular differentiation protocol.

First, we investigated whether hiPSCs seeded onto dSkMs still preserved their pluripotency before the induction of the neuromuscular differentiation (day -1), and then if they were able to exit from pluripotency upon the induction of the neuromuscular differentiation protocol (day2 and day5). Immunofluorescence analysis for the key pluripotent transcription factors octamer-binding transcription factor 4 (OCT4) and homeobox protein NANOG showed that hiPSCs cultured onto dSkM preserved their pluripotency before the induction of the neuromuscular differentiation (Fig. 1c, d, Supplementary Fig. 1a, b and Supplementary Table 1). Differently, cells seeded onto dSkM exited from pluripotency at 2 and 5 days after the supplementation of neuromuscular differentiation media, as shown by the quantification of $OCT4^+NANOG^+$ cells (Fig. 1c, d). To understand whether loss of pluripotency was associated with hiPSC commitment toward mesodermal and/or neuromesodermal lineages, we further analyzed samples via immunofluorescence staining for the key determinant transcriptional factors mesoderm-induction T-box transcription factor brachyury (TBRA) and SRY-box transcription factor 2 (SOX2)[48–50]. $TBRA^+SOX2^-$ and $TBRA^+SOX2^+$ cells were identified after 2 and 5 days of differentiation, confirming the ability of hiPSCs to differentiate toward mesodermal and/or neuromesodermal lineages, respectively (Fig. 1e–g, Supplementary Fig. 1c and Supplementary Table 2,3). Similar proportions of early cell commitment were obtained for two additional hiPSC lines differentiated in presence of dSkM for 2 days (Supplementary Fig. 1d–f).

Once confirmed that hiPSCs seeded onto dSkM responded to the neuromuscular differentiation protocol, we investigated whether dSkM could sustain the generation of t-NMOs at longer time points of differentiation. We thus followed cell growth onto dSkM during the time of culture in presence of media supplemented with small molecules and growth factors. Morphometric analysis showed that extensive 3D cell aggregates were formed onto the dSkM from day 10 to day 20 of cell culture, and by day 30 cells completely invaded the available surface of dSkMs creating a 3D cell-dSkM construct (Supplementary Fig. 1g). Due to the cell growth observed 30 days after neuromuscular differentiation of multiple hiPSC lines (Supplementary Fig. 1g, h and Supplementary Table 4), we investigated the neuromuscular system at this time point. Whole mount immunofluorescence staining revealed that neuron-specific class III beta-tubulin$^+$ (TUJ-1) and desmin$^+$ myogenic cells were present as discrete neuronal and muscular compartments (Fig. 1h and Supplementary Fig. 2a–d). A significantly higher percentage of myogenic area over the neuronal compartment was revealed in t-NMOs (Fig. 1i). Overall, t-NMOs showed a 3D organization of neural clusters growing onto the dSkM, muscular cells present mainly in the proximity of the dSkM reached by neuritic projections, which also invaded the dSkM scaffold (Fig. 1h, j and Supplementary Fig. 2a–d). Such morphogenesis was characterized by a complex 3D organization of the neuronal network and of myogenic cells (Fig. 1h and Supplementary Fig. 2a), with neuritic extensions projected toward bundles of elongated desmin$^+$ cells (Fig. 1j). Abundant basement membrane ECM component laminins were revealed in the proximity of the dSkM, which was invaded by cells (Supplementary Fig. 2c, d). Cell distribution within the dSkM followed the patterning imposed by the dSkM, as shown by directionality quantification of the cells located in the proximity of decellularized myofibers (Fig. 1k and Supplementary Fig. 2d). Interestingly, t-NMOs showed a rhythmic and spontaneous contraction starting from day 15 of neuromuscular differentiation through the end point of the experiment (Supplementary Movies 1, 2). To quantify such basal activity, we used live imaging analysis of calcein loaded t-NMOs to reveal viable cells and simultaneously monitor cell morphology and spontaneous contraction (Supplementary Movie 1). Whole mount or specific regions of interest (ROIs) of t-NMOs were analyzed to measure the fluorescence intensity variation during the time of live imaging acquisition. By doing so, we were able to visualize and measure peaks of fluorescence intensity corresponding

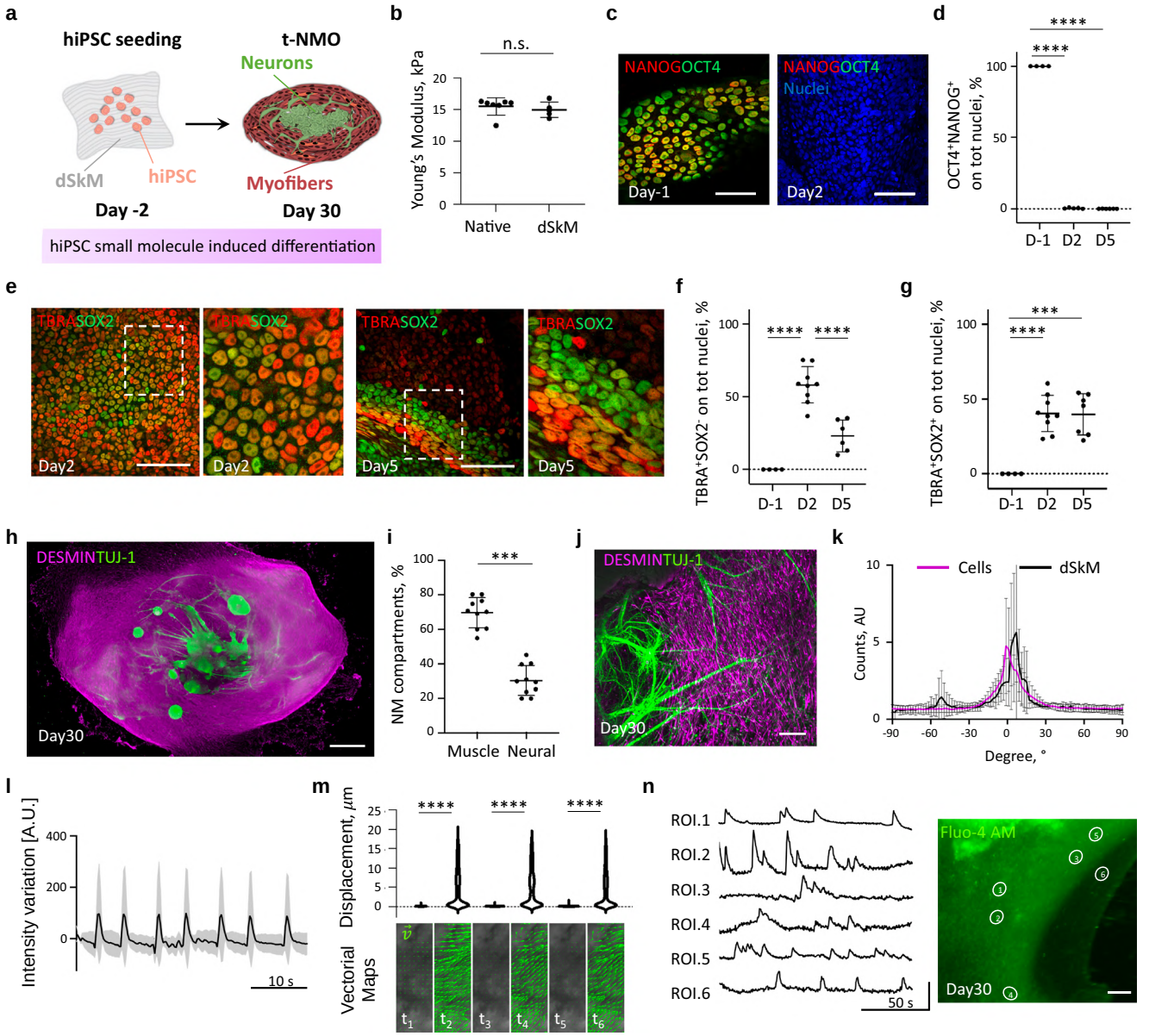

to t-NMO contraction (Fig. 1l, Supplementary Fig. 2e, f and Supplementary Movie 1). Similar results were obtained by analyzing samples via bright field live imaging analysis of t-NMOs (Supplementary Fig. 2g and Supplementary Movie 2). On the same line, when live imaging records were analyzed using a particle image velocimetry software (PIVlab)[51–54], we were able to quantify t-NMO displacements and to generate vectorial maps, confirming spontaneous cycles of contraction and relaxation of t-NMOs (Fig. 1m). Subsequently, to further investigate the physiological basal activity of t-NMOs, we loaded t-NMOs with the Fluo-4 dye, which allows the monitoring of calcium fluxes[55]. We revealed that t-NMOs displayed basal calcium transients, as shown by the quantification of the Fluo-4 fluorescence intensity variation of multiple ROIs (Fig. 1n).

Overall, these results show that dSkMs support hiPSCs culture and differentiation toward cell types belonging to the neuromuscular system which organized into a functional 3D construct to form t-NMOs.

Myofiber differentiation and functionality is promoted by dSkM

Based on the neuromuscular integration revealed in t-NMO (Fig. 2a, b), we decided to further characterize the myogenic and the neuronal composition of t-NMOs. As first, we assessed spatial distribution and cell identity of myogenic cells in functional t-NMOs, by combining immunofluorescence and gene expression analysis (Fig. 2c–r).

We found that day 30 t-NMOs possess myogenic precursors, as shown by immunofluorescence analysis for paired box 7 (PAX7) transcription factor[5] (Fig. 2c–g). This cell population represents approximately the 10% of the total nuclei present into t-NMO after 30 days of differentiation (Fig. 2d). Moreover, $PAX7^+$ cells identified in t-NMOs were mostly in a non-proliferating state, as shown by their statistically significant higher percentage of $PAX7^+Ki67^-$ cells on total $PAX7^+$ cells, when compared to proliferating $PAX7^+Ki67^+$ cells (Fig. 2e). We also revealed $PAX7^+$ cells located between pre-existing ghost myofibers and basal lamina, occupying the anatomical position that defines the adult muscle stem cells, called satellite cells[23] (Fig. 2f). Next, we assessed the presence of committed and terminally differentiated myogenic cells. We found that 30 days after neuromuscular differentiation, t-NMOs showed committed myogenic cells that are positive for the MYOG transcription factor (Fig. 2g, h) and myosin heavy chain (MYHC) positive myofibers (Fig. 2h). Such myogenic differentiation in presence of dSkM was confirmed for 3 different hiPSC lines, which t-NMOs show similar proportion of $MYOG^+$ and $MYHC^+$ cells upon 30 days of differentiation (Supplementary Fig. 2h, i). In agreement, we also identified elongated and multinucleated cells that display the typical striated

Fig. 1 | DSkMs support hiPSC differentiation into tissue-engineered NMO. **a** Schematic illustration showing the strategy used for t-NMO generation. Scaffolds derived from dSkM were used as substrate for seeding hiPSCs as single cells. Upon 2 days from seeding, cells underwent to a small-molecule based differentiation protocol until day 30 to derive t-NMOs. **b** Scatter dot plot showing the mean of the Young's modulus measured by atomic force microscopy of native freshly isolated murine diaphragms (Native) and decellularized murine diaphragms (dSkM). Data are shown as mean ± s.d. of 5–7 independent biological replicates; unequal variance Student's t-test; n.s., not statistically significant. **c** Z-stack confocal immunofluorescence imaging showing hiPSCs co-expressing NANOG (red) and OCT4 (green) 48 h (Day-1) after hiPSCs seeding onto the dSkM and 72 (D2) hours from hiPCs differentiation. Scale bars, 100 µm. **d** Scatter dot plot showing the percentage of $OCT4^+$ $NANOG^+$ cells on the total amount of nuclei after 48 h from hiPSCs seeding (D-1) and 72 (D2) and 120 (D5) hours from hiPCs differentiation. Data are shown as mean ± s.d. of 4–6 independent biological replicates from two differentiation experiments, at least 4500 nuclei were counted per each time point; one-way ANOVA with Tukey's multiple comparisons test, $^{****}P < 0.0001$. Statistical results are reported in Supplementary Table 1. **e** Z-stack confocal immunofluorescence images showing cells expressing TBRA (red) and SOX2 (green) after 2 (Day2) and 5 (Day5) days from hiPSC differentiation onto dSkM. Scale bars, 50 µm. **f** Scatter dot plot showing the percentage of $TBRA^+SOX2^-$ progenitors after 48 h from hiPSCs seeding (D-1) and after 2 (D2) and 5 (D5) days from hiPSCs differentiation. Data are shown as mean ± s.d. of 4, 9 and 6 independent biological replicates from at least two differentiation experiments, at least 6000 nuclei were counted per each time point; One-way ANOVA with Tukey's multiple comparisons test, $^{****}P < 0.0001$. Statistical results are reported in Supplementary Table 2. **g** Scatter dot plot showing the percentage of $TBRA^+SOX2^+$ progenitors after 48 h from hiPSCs seeding (D-1) and after 2 (D2) and 5 (D5) days from hiPSCs differentiation. Data are shown as mean ± s.d. of 4, 9 and 7 independent biological replicates, from at least two independent experiments, and at least 6000 nuclei were counted per each time point; One-way ANOVA with Tukey's multiple comparisons test, $^{****}P < 0.0001$. Statistical results are reported in Supplementary Table 3. **h** Representative stereomicroscope immunofluorescence image showing whole mount t-NMO stained for desmin (magenta) and TUJ-1 (green) after 30 days of hiPSC differentiation. Scale bar, 2 mm. **i** Scatter dot plot showing the mean of the area occupied by muscular (desmin positive) or neuronal (TUJ-1 positive) cells in t-NMO after 30 days of differentiation, expressed as percentage on the total neuromuscular area. Data are shown as mean ± s.d. of 10 independent biological replicates, 4 derived from BJ1-hiPSCs, 3 from BJ2- and 3 from BJ3-hiPSCs. Each hiPSC line was used for an independent t-NMO differentiation experiment; dots represent a single biological replicate; unequal variance Student's t-test; n.s., $^{***}P = 0.0008$. **j** Representative Z-stack confocal immunofluorescence image of whole mount t-NMO stained for desmin (magenta) and TUJ-1 (green) after 30 days of differentiation. Scale bar, 200 µm. **k** Quantification of cellular and dSkM ghost myofiber directionality. Data are shown as mean ± s.d. of 3 independent biological replicates from one differentiation experiment. **l** Mean normalized fluorescence intensity variation of contracting t-NMOs loaded with calcein registered during live imaging acquisition with a fluorescent stereomicroscope. Images were processed with Spiky and analyzed with MATLAB. Data are shown as mean ± s.d. of 3 independent biological replicates from three independent differentiation experiments; A.U., arbitrary unit. **m** Upper panel, violin plot showing the maximum displacement of a representative t-NMO reported in L from one differentiation experiment and measured during 3 cycles of contraction - relaxation (t_1 *vs* t_2, t_3 *vs* t_4, t_5 *vs* t_6) using PIVlab. The analysis was performed considering the identical query region per each time point analyzed (number of analyzed vectors per each time point: 4870). Unequal variance Student's t-test was used; $^{****}P < 0.0001$. Lower panel, representative vector maps generated by comparing pairs of frames selected before contraction (t_1, t_3, t_5) or at the maximum of sample contraction (t_2, t_4, t_6). **n** Left panel, representative charts of peak amplitude spectrum ($\Delta F/F_0$) basal activity of t-NMO loaded with Fluo-4 and analyzed with live fluorescence imaging after 30 days from hiPSCs differentiation to reveal calcium transients. Data are shown as independent ROI of a single sample. Right panel, representative single frame of live imaged (Fluo-4) cells in t-NMO after 30 days of differentiation used for calcium live imaging analysis. Scale bar, 200 µm.

pattern of myofiber cytoskeleton, as shown by slow or fast MYHC isoform immunostainings and F-actin organization (Fig. 2i and Supplementary Fig. 2b).

To investigate whether dSkMs could promote skeletal muscle differentiation of hiPSCs, as it does for adult muscle precursor cells[30], we induced hiPSC neuromuscular differentiation in absence of dSkM (Supplementary Fig. 3a–d). Thirty days after differentiation, samples derived without dSkM presented both neuronal and muscular cell types (Supplementary Fig. 3b–e), with clusters of neural cells ($TUJ\text{-}1^+$) that extended projections toward $desmin^+$ myogenic cells (Supplementary Fig. 3b, c). We then used morphometric and gene expression analysis to compare neuromuscular in vitro models (day 30) derived in presence of dSkM (i.e. t-NMO) with those obtained in absence of dSkMs. We found significant increase of *MYOG* and *MHC* expression in t-NMOs, when compared to hiPSCs differentiated in absence of dSkMs (Supplementary Fig. 3f), supporting the hypothesis that dSkM could improve myofiber differentiation. To further investigate such aspect, bulk RNA-sequencing analysis was performed 30 days after differentiation of hiPSCs cultured in presence or in absence of dSkMs (Fig. 2j–n, Supplementary Data 1 and 2). According to the differentiation protocol applied, 30 days after differentiation hiPSC-derived cells expressed muscle score genes[47] (Supplementary Fig. 3g), as well as sets of genes belonging to neural cells (including neurons and Schwann cells) and mesenchymal cells (Supplementary Fig. 3h). Despite some similarities, principal component analysis (PCA) showed that hiPSCs differentiated in presence or in absence of dSkMs were transcriptionally well distinguishable (Fig. 2j), as confirmed by the 1605 differentially expressed genes (DEGs; Supplementary Data 1). More in detail, we found that t-NMOs showed downregulation of genes annotated within the categories related to development, including nervous system development, when compared to samples derived in absence of dSkM (Fig. 2k and Supplementary Data 2). Moreover, t-NMOs showed downregulation of genes belonging to ECM production and remodeling, when compared to samples derived in absence of dSkM, suggesting an active contribution of the ECM provided by the dSkM in t-NMOs or a differential timing of ECM gene expression (Fig. 2k and Supplementary Fig. 3i). On the contrary, t-NMOs overexpressed genes associated with "Regulation of Metabolic Processes" and "RNA metabolism and translation" categories, when compared to samples obtained in absence of dSkMs (Fig. 2k and Supplementary Data 2). Notably, t-NMOs also showed upregulation of genes involved in skeletal muscle contraction, when compared to hiPSCs differentiated in absence of dSkMs (Fig. 2k, l and Supplementary Data 2). Accordingly, DEGs annotated within "skeletal muscle contraction" category in Reactome database were upregulated in t-NMOs, when compared to samples derived in absence of dSkMs (Fig. 2l, m). The same was observed for a list of manually annotated DEGs related to myofiber cytoskeleton components (Fig. 2n). In particular, t-NMOs highly overexpressed titin, actin, troponin and myosin genes, including neonatal and adult myosin heavy chain (MYH) gene isoforms *MYH8* and *MYH2*[56], respectively (Fig. 2n).

Such a higher degree of myogenic differentiation revealed at transcriptional level in t-NMOs was further confirmed by morphometric analysis. We found a statistically significant higher number of oriented, longer and thicker myofibers in t-NMOs, when compared to neuromuscular system in vitro models derived in absence of dSkM (Fig. 2o, p and Supplementary Fig. 3j). Neither cardiac nor smooth muscle cells were detected in the t-NMOs (Supplementary Fig. 4a–c), while we identified muscular supporting cell types expressing the muscular fibroblast marker TE7[57] (Supplementary Fig. 4d, e). Finally, to confirm that the improved maturation of skeletal muscle in t-NMOs was associated to an enhanced functional phenotype, we performed live imaging analysis of samples derived in absence or in presence of dSkM upon acetylcholine (ACh) administration to evaluate muscle contraction and calcium spikes. We found that t-NMOs displayed higher degree of muscle contraction and improved response to calcium spikes upon ACh stimulation, when compared to neuromuscular system in vitro models derived in absence of dSkM (Fig. 2q, r).

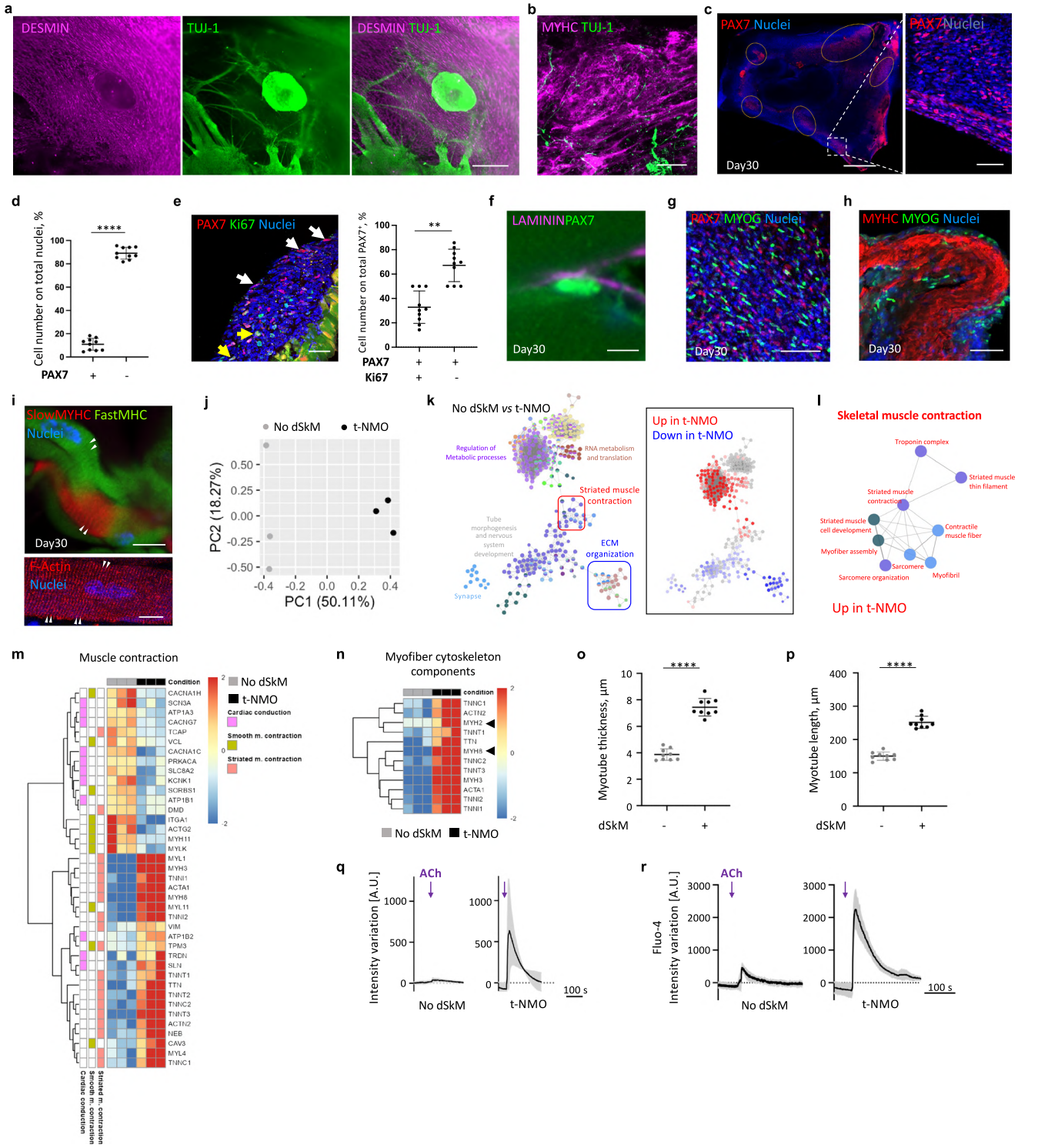

Overall, these data showed that dSkM supports the derivation of multiple muscular cell types in t-NMOs derived from hiPSCs, and promotes skeletal muscle maturation and function.

t-NMOs possess multiple neural cell types and show complex extension of neuritic projections

As previously shown, day 30 t-NMOs displayed not only cells belonging to the skeletal muscle but also to the neural compartment, whose neuritic projections reached bundles of terminally differentiated muscular cells (Fig. 3a, b). To analyze the neural compartment of t-NMOs, we combined immunofluorescence, morphometric and gene expression analyses. We found that both neural progenitors and mature neurons were present in t-NMOs, as shown by immunofluorescence analysis that revealed cells co-expressing paired Box 6 nuclear factor (PAX6) and SOX2[58] (Fig. 3c and Supplementary Fig. 5a), or neuronal nuclear protein (NEUN) and microtubule-associated protein 2 (MAP2)[59], respectively (Fig. 3d and Supplementary Fig. 5b). Mature neurons ($NEUN^+$) were present in t-NMOs with statistically significant higher proportion when compared to neural progenitors ($PAX6^+SOX2^+$; Fig. 3e). In addition, we observed a specific distribution among the neuronal cell populations, where mature neurons localized in close proximity to the dSkM, while neural progenitors were identified in regions more distant from the dSkM (Fig. 3f).

Fig. 2 | Characterization of the myogenic compartment of day 30 t-NMOs. **a** Representative stereomicroscope image showing muscular and neural integration in t-NMO by whole mount immunofluorescence staining for desmin (magenta) and TUJ-1 (green). Scale bar, 500 µm. **b** Representative confocal Z-stack image of t-NMO stained for TUJ-1 (green) and MYHC (magenta). Scale bar, 400 µm. **c** Representative confocal Z-stack image showing whole mount immunofluorescence staining for PAX7 (red). Nuclei were stained with Hoechst (blue). Scale bars, 1 mm (left) and 100 µm (right). **d** Scatter dot plot showing the mean number of PAX7-positive (+) and of PAX7-negative (–) cells, expressed as percentage on the total nuclei acquired per image (≥100 nuclei per image). Data are shown as mean ± s.d. of 10 independent biological replicates, 4 derived from BJ1-hiPSCs, 3 from BJ2- and 3 from BJ3-hiPSCs. Each hiPSC line was used for an independent t-NMO differentiation experiment; dots represent a single biological replicate; unequal variance Student's t-test was used; $^{****}P < 0.0001$. **e** Left panel, representative confocal Z-stack images showing immunofluorescence staining that identify $PAX7^{+}Ki67^{-}$ (white arrows) and $PAX7^{+}Ki67^{+}$ (yellow arrows) cells. Scale bar, 50 µm. Right panel, scatter dot plot showing the mean of PAX7 positive cells (+) that do not co-express (–) or co-express (+) the proliferating marker Ki67, expressed as percentage on total $PAX7^{+}$ cells (a total of ≥ 200 PAX7+ cells were analyzed). Data are shown as mean ± s.d. of 10 independent biological replicates, 4 derived from BJ1-hiPSCs, 3 from BJ2- or 3 from BJ3-hiPSCs. Each hiPSC line was used for an independent t-NMO differentiation experiment; dots represent a single biological replicate; unequal variance Student's t-test was used; $^{**}P = 0.0027$. **f.** Representative confocal Z-stack image showing immunofluorescence staining for PAX7 (green) and laminin (magenta). Scale bar, 10 µm. **g** Representative image showing immunofluorescence staining for MYOG (green) and PAX7 (red) of t-NMO cryo-sections. Nuclei were stained with Hoechst (blue). Scale bar, 200 µm. **h** Representative confocal Z-stack image of t-NMO immunostained for MYHC (red) and MYOG (green). Nuclei were stained with Hoechst (blue). Scale bar, 50 µm. **i** Representative confocal Z-stack images of t-NMO immunofluorescence analysis of myofibers showing sarcomeric organization (white arrowheads) of fast and slow MYHCs (upper) and F-actin (lower). Nuclei were stained with Hoechst (blue). Scale bars, 10 µm. **j** Principal component analysis (PCA) of samples obtained in presence (t-NMO, black) or in absence of dSkM (No dSkM, gray). Each dot represents a single biological replicate. **k** Left, enrichment analysis of differentially expressed genes between samples obtained in presence (t-NMO) or in absence of dSkM (No dSkM), within Gene Ontology and Reactome databases. Dot colors in the network highlight groups of categories with overlapping genes. Right, inset represents the same network where dots are colored according to the percentage of genes within each category that have positive (red) or negative (blue) log-fold change of gene expression. **l** Enlargement of the portion of network highlighted in (**k**), with categories related to skeletal muscle contraction, which are upregulated in samples obtained in presence of dSkM (t-NMO), when compared to those derived in absence of dSkM (No dSkM). **m** Hierarchical clustering with heatmap visualization of DEGs within the Reactome Muscle Contraction category. **n** Hierarchical clustering with heatmap visualization of manually annotated DEGs identifying myofiber cytoskeleton components. Arrows point at the adult *MYH2* and neonatal *MYH8* genes. **o** Scatter dot plot showing the mean thickness of $desmin^{+}$ myotube cross-section in samples derived in absence (–) or in presence (+) of dSkM. Data are shown as mean ± s.d. of 9 independent biological replicates per experimental condition, 3 derived from BJ1-, 3 from BJ2- and 3 from BJ3-hiPSCs. Each hiPSC line was used for an independent differentiation experiment; each dot represents the mean of 30 myotubes per each biological replicate; unequal variance Student's t-test was used; $^{****}P < 0.0001$. **p** Scatter dot plot showing the mean length of $desmin^{+}$ myotube in whole mount samples derived in absence (–) or in presence (+) of dSkM. Data are shown as mean ± s.d. of 9 independent biological replicates per experimental condition, 3 derived from BJ1-, 3 from BJ2- and 3 from BJ3-hiPSCs. Each hiPSC line was used for an independent differentiation experiment; each dot represents the mean of 30 myotubes per each biological replicate; unequal variance Student's t-test was used; $^{****}P < 0.0001$. **q** Representative quantification of mean normalized fluorescence intensity variation registered during muscle contraction in samples derived in absence (No dSkM) and in presence of dSkM (t-NMO) upon ACh stimulation via live imaging fluorescent stereomicroscope acquisition. Data are shown as mean ± s.d. of 3 independent biological replicates from one differentiation experiment. Dotted lines correspond to the baseline equal to 0. **r** Representative mean of peak amplitude spectrum ($\Delta F/F_0$) of cells in samples derived in absence and in presence of dSkM (t-NMO) and stimulated with ACh. Samples were loaded with Fluo-4 and analyzed with live fluorescence imaging to reveal calcium transients upon ACh stimulation. Data are shown as mean ± s.d. of 7 or 3 independent biological replicates from one differentiation experiment.

Thus, we further investigated the nature of the mature neurons present in t-NMOs after 30 days of differentiation. Quantitative PCR analysis showed expression of the specific neuronal transcription factors, such as LIM/homeodomain family of transcription factors *ISLET1*[58] and MN-determinant homeobox gene *MNX1*[60] (a.k.a. *HB9*), with statistically significant overexpression in samples derived in presence of dSkM, when compared to those obtained in absence of dSkM (Supplementary Fig. 5c, d). Immunofluorescence analysis performed in t-NMOs confirmed the presence $MAP2^{+}$ neurons co-expressing ISLET1/2[60], and cells expressing HB9[60] (Supplementary Fig. 5e-g). Accordingly, a small population of choline acetyltransferase (CHAT) positive cells was also identified (Fig. 3g and Supplementary Fig. 5h–k). This finding, combined with the previous observations, strongly suggested the presence of a restricted cohort of MNs in day 30 t-NMOs. Moreover and according to RNA-seq analysis, we also found supporting cell types positive for S100 calcium-binding protein B (S100β), a known Schwann cell marker[61], located in close proximity of neuritic projections (Supplementary Fig. 5l, m). Finally, we revealed that in the presence of dSkM neuritic projection length and thickness were significantly increased, when compared to in vitro models obtained in absence of dSkM (Fig. 3h–j).

Altogether, these results show that dSkM supports the maintenance of different neuronal cell types, and the generation of a complex network of neuritic projections in t-NMOs.

T-NMOs present NMJ elements and functional neuromuscular interaction

Since our results showed the presence of key cell types of the human neuromuscular system, we then investigated whether t-NMOs possess NMJs and a functional interaction between the muscular and neural compartments after 30 days of hiPSC differentiation could be revealed. We first assessed the presence of NMJs by investigating pre- and post-synaptic elements via imaging analysis. Fluorescent alpha-bungarotoxin (BTX) staining identified AChR clusters (Fig. 4a). Moreover, we found that ECM components known to support NMJ structural and functional integrity as collagen VI and perlecan[27,28] were deposited in the proximity of AChR clusters (Fig. 4b). The presence of neuritic projections positive for TUJ-1 or for synaptic vesicle glycoprotein 2 (SV2) located in the proximity of AChR clusters suggested the presence of functional NMJs (Fig. 4c and Supplementary Fig. 6a–d). Electron microscopy analysis also confirmed the presence of myofibers, bundles of neuronal axons and NMJs in t-NMOs (Supplementary Fig. 6e–g). Cells expressing the S100β Schwann cell marker were also found in the proximity of clustered AChRs contacted by neuronal extensions (Supplementary Fig. 6h). We found that the number of AChR clusters reached by SV2 neuronal projections was significantly increased in t-NMOs, when compared to samples obtained in absence of dSkM (Fig. 4d and Supplementary Fig. 6i). Accordingly, quantitative PCR gene expression analysis showed that the adult[62,63] epsilon isoform (*AChRε*) of the AChR was significantly upregulated in t-NMOs with respect to the fetal[62,63] *AChR* gamma isoform (*AChRγ*, Fig. 4e). In agreement, upon neuronal stimulation with glutamate (Glu), muscle contraction was clearly evoked only in t-NMOs, when compared to samples derived in absence of dSkM (Fig. 4f, Supplementary Fig. 6j, Supplementary Movies 3 and 4). To assess that Glu-mediated t-NMO contraction was triggered by a functional neuromuscular connection, we used botulinum neurotoxin A (BoNTA) and BTX to induce pre-synaptic[64] or post-synaptic[65] block of the NMJ, respectively. To do so, t-NMO contraction was measured via live imaging analysis before and after 12 h of treatment with BoNTA or BTX. As a control, we analyzed t-NMO contraction in the absence of toxins at the same time points (0 and 12 h). As expected in a functional neuromuscular system[64,65], both toxins inhibited muscle contraction of t-NMO upon Glu-mediated neuronal stimulation (Fig. 4g–i, Supplementary Fig. 6j and Supplementary Table 5). Live imaging analysis revealed that t-NMOs responded to Glu stimulation with calcium spikes in the muscular

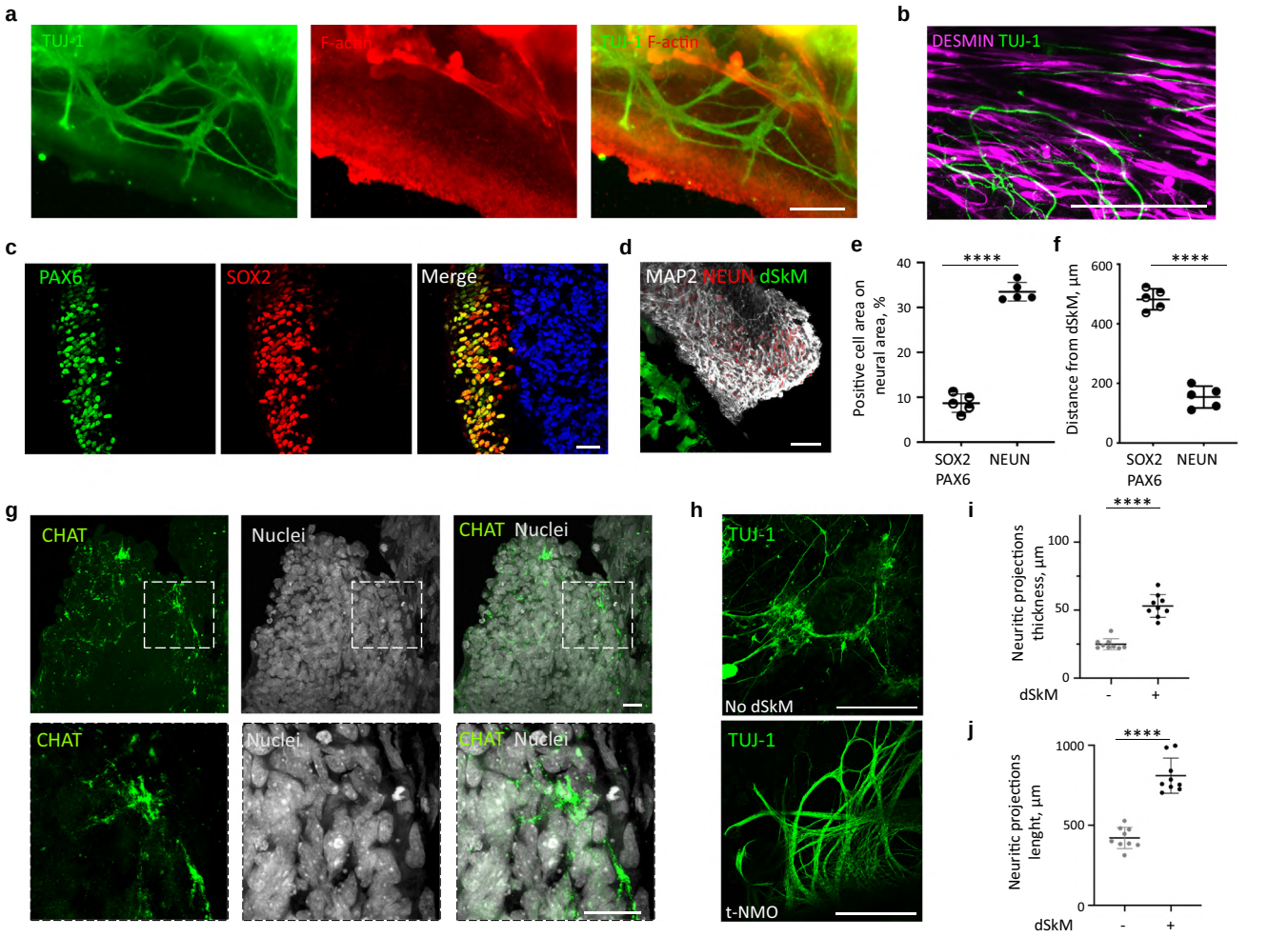

Fig. 3 | Characterization of the neuronal compartment in day 30 t-NMOs. **a** Representative stereomicroscope images showing neural network integration in t-NMOs stained in whole mount immunofluorescence for TUJ-1 (green) and actin (red). Scale bar, 200 µm. **b** Representative confocal Z-stack image of whole mount t-NMO immunostained for desmin (magenta) and TUJ-1 (green). Scale bar, 400 µm. **c** Representative confocal Z-stack images showing neural progenitor cells co-expressing PAX6 (green) and SOX2 (red). Scale bar, 40 µm. **d** Representative confocal Z-stack images showing immunofluorescence staining of t-NMOs for the mature neuron markers NEUN (red) and MAP2 (white). Scale bar, 50 µm. **e** Scatter dot plot showing the area of neural progenitors (co-expressing SOX2 and PAX6) or of $NEUN^+$ cells on the total neuronal area. Data are shown as mean ± s.d. of 5 independent biological replicates from two independent differentiation experiments, at least 982 nuclei were counted per each replicate and dots represent single biological replicates; unequal variance Student's t-test was used; $^{****}P < 0.0001$. **f** Scatter dot plot showing the mean distance of $PAX6^+SOX2^+$ neural progenitors or $NEUN^+$ neurons from the dSkM in t-NMO cross-sections. Data are shown as mean ± s.d. of 5 independent biological replicates from two independent differentiation experiments, at least 30 measures were counted per each replicate and dots represent single biological replicates; unequal variance Student's t-test was used; $^{****}P < 0.0001$. **g** Upper panels, representative confocal Z-stack images showing immunofluorescence staining of t-NMOs for the MN marker CHAT (green) and nuclei (white). Inserts with higher magnification images are reported in the lower panels. Scale bars, 20 µm. **h** Representative confocal Z-stack images showing TUJ-1 (green) positive neuritic projections in samples obtained in absence (upper panel, No dSkM) or in presence (lower panel, t-NMO) of dSkM. Scale bars, 500 µm. **i** Scatter dot plot showing the mean thickness (cross-section) of TUJ-1 positive neuritic projections in samples obtained in absence (–) or in presence (+) of dSkM. Data are shown as mean ± s.d. of 9 independent biological replicates per each experimental condition, 3 derived from BJ1-, 3 from BJ2- and 3 from BJ3-hiPSCs. Each hiPSC line was used for an independent differentiation experiment; each dot represents the mean of 30 neuritic projections measured per each biological replicate; $^{****}P < 0.0001$. **j** Scatter dot plot showing the mean length of TUJ-1 positive neuritic projections in samples obtained in absence (–) or in presence (+) of dSkM. Data are shown as mean ± s.d. of 9 independent biological replicates per each experimental condition, 3 derived from BJ1-, 3 from BJ2- and 3 from BJ3-hiPSCs. Each hiPSC line was used for an independent differentiation experiment; each dot represents the mean of 30 neuritic projections measured per each biological replicate; unequal variance Student's t-test was used; $^{****}P < 0.0001$.

compartment during contraction (Fig. 4j and Supplementary Movie 3). We confirmed that this calcium response was due to a functional neuromuscular connection, as shown by the statistically significant reduction of the normalized peak of Fluo-4 intensity variation in the muscular areas upon Glu stimulation in toxin-treated t-NMOs, when compared to untreated t-NMOs (Fig. 4k and Supplementary Table 6).

Altogether, these data indicate that t-NMOs possess NMJ elements and a functional neuromuscular interaction 30 days after hiPSC differentiation, allowing the study of skeletal muscle activity upon neuronal stimulation.

DMD-derived t-NMOs display altered muscular activity upon neurotransmitter stimulation

After we characterized the morphological and functional features of t-NMOs, we investigated whether t-NMO technology could reveal altered muscular physiology upon neuronal activation and be used to model skeletal muscle diseases. As proof of principle, we derived and studied in parallel t-NMOs produced with hiPSCs reprogrammed from human foreskin fibroblast cell line (BJ; when not specified, named t-NMO, Figs. 1–5), from 3 healthy donors (HD1-3) and from 4 DMD patients (Fig. 5a and Supplementary Fig. 7, 8).

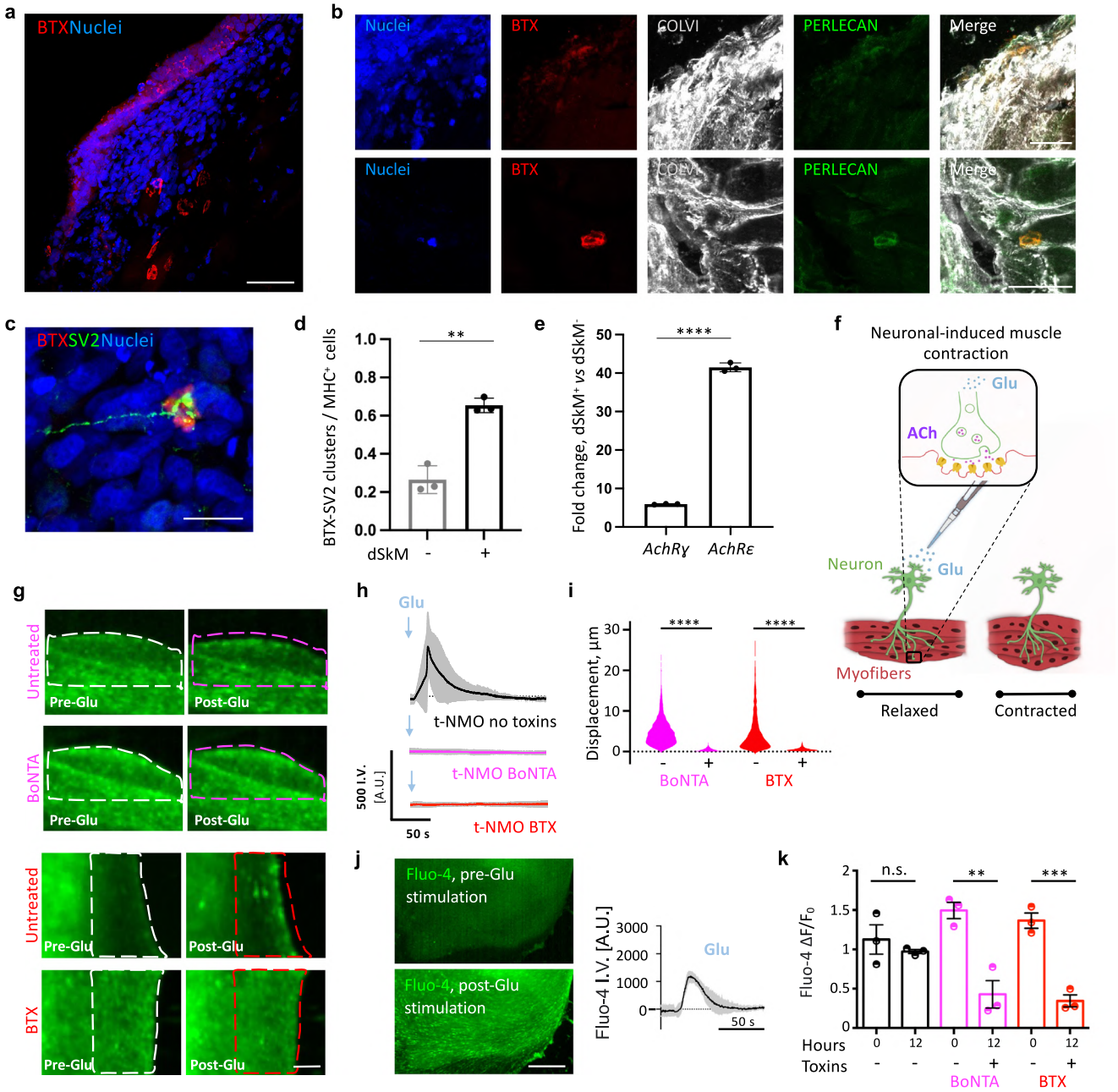

As for the hiPSCs produced from the BJ line, we used the fast and highly efficient method of microfluidic cell reprogramming technology[66] to initially generate DMD1 hiPSCs from a DMD patient-derived primary cell culture, carrying a stop codon mutation that leads to the loss of dystrophin production[41] (Supplementary Fig. 7a). We then applied the same neuromuscular differentiation protocol to first derive and analyze day 30 t-NMOs from DMD1 hiPSCs. DMD1 t-NMOs showed similar cellular growth, 3D organization and neuromuscular compartmentalization observed previously in t-NMOs (Fig. 5b and Supplementary Fig. 7b, c). Next, we confirmed by immunofluorescence that the dystrophin protein was absent in the muscular compartment and that NMJ elements were present in DMD1 t-NMOs upon 30 days of differentiation (Supplementary Fig. 7d, e). Bulk RNA-sequencing analysis was performed to evaluate gene expression profile changes of DMD1 t-NMOs, when compared to t-NMOs. PCA analysis showed that DMD1 t-NMOs clustered separately from t-NMOs only along the second principal component (Fig. 5c). Only 21 DEGs were significantly up-regulated in t-NMOs and 25 down-regulated in t-NMOs, when compared to DMD1 t-NMOs (Supplementary Data 3).

Once confirmed that DMD1 t-NMOs showed a similar neuromuscular differentiation profile of that observed in t-NMOs, we then included in the study hiPSCs generated from three HDs (HD1, HD2, HD3) and other three DMD patients (DMD2, DMD3 and DMD4; Supplementary Fig. 8a, b). We confirmed that the neuromuscular commitment in presence of dSkM of HD1-3 and DMD1-4 hiPSC lines was similar among the different hiPSC lines used in this study (Supplementary Fig. 8c–e, Supplementary Table 7 and Supplementary Table 8). Thirty days after neuromuscular differentiation, t-NMOs were derived from all the HD and DMD hiPSCs, showing similar cell growth and neuromuscular system organization (Supplementary Fig. 7b, c and Supplementary Fig. 8f). Importantly, the proportion between neuronal and muscular compartments observed within t-NMOs produced with hiPSCs derived from 3 BJ lines, 3 HDs and 4 DMD patients was similar, with a significantly higher proportion of muscular compartment over the neuronal one (Fig. 5d, e and Supplementary Table 9). Accordingly, gene expression analysis for *CHAT* gene was similar among the t-NMOs derived from the different hiPSC lines (Supplementary Fig. 8g and

Fig. 4 | t-NMOs show NMJ elements and functional neuromuscular interaction 30 days after hiPSC differentiation. a Representative immunofluorescence image showing α-bungarotoxin$^+$ (BTX, red) regions in t-NMO. Nuclei were stained with Hoechst (blue). Scale bar, 50 µm. **b** Representative immunofluorescence images showing BTX$^+$ (red) regions localization within ECM stained for collagen VI (COLVI, gray) and proteoglycans (Perlecan, green). Nuclei were stained with Hoechst (blue). Scale bars, 25 µm. **c** Representative immunofluorescence image of BTX$^+$ (red) regions found in close contact with SV2$^+$ neuritic projections (green). Scale bar, 20 µm. **d** Quantification of BTX$^+$ clusters contacted by SV2$^+$ neuritic projections (BTX-SV2 clusters). Data are normalized for the number of MHC$^+$ cells, and shown as mean ± s.d. of 3 independent biological replicates from a single differentiation experiment. Unequal variance Student's t-test was used; $^{**}P = 0.012$. **e** *AChR* γ and ε subunit gene expression in t-NMOs. Data are normalized to *MHC* gene expression and displayed as fold change over the samples derived in absence of dSkM. Data are shown as mean ± s.d. of 3 independent biological replicates from a single differentiation experiment. Unequal variance Student's t-test was used; $^{****}P < 0.001$. **f** Schematic illustration showing the strategy used for testing neuromusuclar function in t-NMO. Glutamate (Glu) was supplemented to induce neural-mediated release of acetylcholine (ACh) and muscle response (NMJ, neuromuscular junction). **g** Representative images showing displacement of t-NMO after Glu stimulation before (untreated) and after 12 h of treatment with BoNTA or BTX. Dotted lines are used to better visualize t-NMO displacement. Scale bar, 150 µm. **h** Representative quantification of normalized fluorescence intensity variation registered during contraction of t-NMOs stimulated with Glu after 12 h of treatment with BoNTA or BTX. As control, t-NMOs not treated with neurotoxins were analyzed (t-NMO no toxins). Data are shown as mean ± s.d. of 3 independent biological replicates from a single differentiation experiment. Dotted lines correspond to the baseline equal to 0. **i** Violin plot showing the maximum displacement of t-NMOs upon Glu stimulation before (−) and after (+) 12 h of treatment with BoNTA or BTX using PIVlab. Each violin represents the displacement vectors obtained from 3 biological replicates per each experimental condition generated from a single differentiation experiment (vector number analyzed ≥3147 per each experimental condition). One-way ANOVA with Tukey's multiple comparisons test was used, $^{****}P < 0.001$. Statistical results are reported in Supplementary Table 7. **j** Left panel, representative images of t-NMO loaded with Fluo-4 before (pre-Glu) and after (post-Glu) Glu stimulation. Scale bar, 500 µm. Right panel, representative mean of Fluo-4 fluorescence intensity variation during time of live imaging acquisition in t-NMOs upon Glu stimulation. Dotted lines correspond to the baseline normalized to 0. In the right panel, data are shown as mean ± s.d. of 3 independent biological replicates. **k** Quantification of calcium peak amplitude ($\Delta F/F_0$) detected with Fluo-4 live imaging analysis upon Glu stimulation of t-NMOs before (i.e., 0 h from treatment; −) or after 12 h of treatment (+) with BoNTA or BTX. As control, t-NMOs not treated with neurotoxins were analyzed at 0 and 12 h (−). The fluorescence intensity peak (F) registered during stimulation was measured and normalized to the baseline fluorescence intensity registered before neurotransmitter stimulation (F0). Data are shown as mean ± s.d. of 3 independent biological replicates from a single differentiation experiment. One-way ANOVA with Tukey's multiple comparisons test, n.s. not significant, $^{**}P = 0.0006$, $^{***}P = 0.0009$. Statistical results are reported in Supplementary Table 8.

Supplementary Table 10). By using western blot analysis, we confirmed that all DMD t-NMOs and dSkM did not present dystrophin protein, when compared to control t-NMOs (BJ1 or HD1-3 t-NMOs; Fig. 5f and Supplementary Fig. 8h). Based on these results, we then investigated DMD1, DMD2, DMD3 and DMD4 t-NMOs functionality, when compared to t-NMOs produced with hiPSCs derived from the 3 different BJ lines or the 3 HDs. According to our previous results, we found that upon neuronal-induced Glu stimulation not only DMD1 t-NMOs, but also all the other DMD t-NMOs showed reduced muscle contraction, when compared to BJ and to HD t-NMOs (Fig. 5g-i, Supplementary Fig. 8i–j, Supplementary Movie 5 and Supplementary Table 11). Moreover, significantly reduced calcium spikes were observed in all DMD t-NMOs, when compared to dystrophin expressing t-NMOs (BJ1 and HD1-3) upon both Glu and ACh neurotransmitter stimulations (Fig. 5j, Supplementary Fig. 8k and Supplementary Table 12). Finally, we found that DMD t-NMOs displayed altered calcium flux upon ACh stimulation, as shown by the inability to completely return to the baseline during the time of calcium live imaging acquisition, when compared to HD t-NMOs (Fig. 5k).

Altogether, these data show that dSkM can be used to generate patient-specific t-NMOs, and to mimic typical DMD skeletal muscle alterations.

Discussion

In the last decades, complex 3D models of the human NM system have been developed in vitro to mimic as much as possible the complex multicellular interaction and structural organization that this system has in vivo[8]. The combination of human pluripotent stem cell technology and tissue engineering approaches has opened new avenues for the generation of human neuromuscular system in vitro models.

Human neuromuscular organoids (NMOs) have been recently derived from both embryonic stem cells or hiPSCs, enabling the production of in vitro models containing isogenic muscular and neuronal compartments[1,3–5,7,8,46]. By using small molecules and growth factors that mimic in vitro signaling pathways involved in vivo during the early events of neuromesodermal specification[48–50], cells self-assemble into spheroids and can be differentiated in vitro into multiple cell types of the NM system[3,5,46]. Despite bioengineering approaches represent a step forward in the translation of organoid technology[67,68], so far no studies reported the use of ECM scaffolds, such as dSkMs, for the generation of tissue-engineered NMO models. Both during developmental and in the adult stages, the ECM of the innervated skeletal muscle serves as a biologically active environment required for the generation and the functional integration of multiple cell types, which guarantees a specific 3D shape and function to the organ[17,18,20,23,28,69].

Here, we took advantage from the dSkMs to derive functional t-NMOs with multiscale 3D organization of myofibers and associated neuronal network. According to organoid definition[68], our hiPSC-derived tissue-engineered in vitro model included multiple cell types typical of the neuromuscular system. When compared to other studies reporting the generation of organoids that reproduced the human neuromuscular system[3,5], t-NMOs did not require pre-differentiation and isolation steps of progenitors derived from hiPSCs, rather hiPSCs were directly seeded and differentiated onto dSkMs. We found that at early stages of differentiation hiPSCs are committed toward neuromesodermal and mesodermal progenitors. We observed that neuromesodermal specification could be obtained without the administration of specific neuralizing factors, as the retinoic acid. Moreover, non-spheric and handleable t-NMOs gave access to easy investigation of the models via live imaging analysis, allowing the study of physiological relevant events at the desired time point during the cell culture.

We showed that basal muscle contraction and calcium transients can be revealed and quantified in t-NMOs using imaging analysis. According to other studies[3,7], we observed variable basal physiological activity in t-NMOs differentiated for 30 days, suggesting a spectra of maturation levels of the muscular compartment. However, at this time point of hiPSCs differentiation, t-NMO showed neuromuscular compartmentalization, with an extensive network of neuritic projections that reached oriented myofiber bundles. Aside from serving as a scaffolding biomaterial for myofibers and neuritic sprouting, dSkMs were also invaded by cells, with some nuclei that repopulated dSkM myofibers or PAX7-expressing cells that localized in the satellite cell position. These results are in agreement with previous in vitro and in vivo studies, where adult stem cells or adult progenitors were shown to invade and repopulate the ghost dSkM with anatomically matched-differentiated cells[29–34]. Altogether, these data support the hypothesis that dSkMs could have a role in promoting cell homing. Despite further investigations are needed, the identification of key ECM elements able to drive human cell homing remains an intriguing biological matter that can open new strategies for engineering specific niches of the human neuromuscular system.

With the aim to better characterize t-NMOs, we then proceeded with further investigation of the muscular and neural compartments

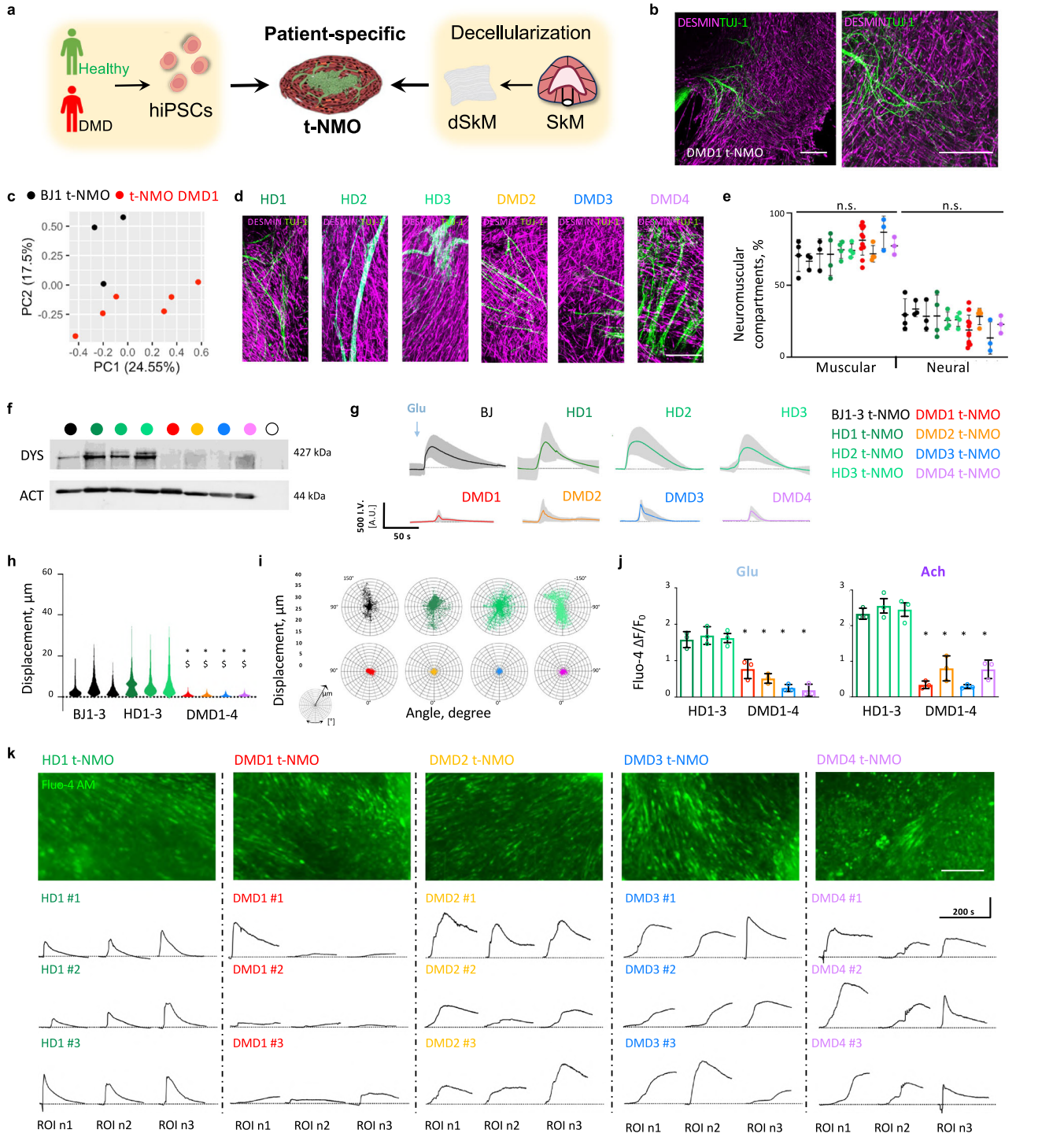

combining immunofluorescence, morphometric and gene expression analyses. Previous studies showed that multiple cell types belonging to the neuromuscular system can be derived from hiPSC differentiated in conventional devices[1,47] or used to generate spheroids[1,3–5,7,8,46]. We detected terminally differentiated myofibers and neurons together with myogenic and neuronal stem cells, and fibroblasts and Schwann cell supporting cell types in day 30 t-NMOs. These observations are consistent with the generation of organoids composed of heterogeneous cell populations proper of the neuromuscular system[1,3–5,7,8,46]. Administration of agonists for the ventralizing morphogen SHH and/or the neuralizing factor retinoic acid could be a future strategy to adopt during t-NMO derivation to further sustain the generation and maturation of MNs from progenitors[1].

To understand whether dSkMs could have an influence on cell differentiation and maturation, we compared samples derived from hiPSCs cultured in presence of dSkM with those obtained in absence of dSkM. It was reported that dSkMs possess pro-myogenic and neurotrophic properties both in vivo and in vitro[29–34]. We found that key genes belonging to terminally differentiated cells, such as those of myofibers and of neurons, were upregulated when hiPSCs were differentiated in the presence of dSkMs for 30 days. Different studies have also reported the use of engineered constructs in which the myofibers are stabilized with synthetic structures, that can be applied to hiPSC-derived cells[70–72]. More generally, by providing a 3D environment to myogenic cells in vitro, muscle maturation can be improved[6]. Moreover, it was also shown that increased neuronal axon sprouting can be involved in the neuronal maturation process[73]. Our data

Fig. 5 | DMD t-NMOs reproduce dysfunctional activity of the skeletal muscle compartment 30 days after hiPSC-differentiation. a Schematic illustration showing the strategy used for producing patient specific t-NMOs from healthy donors (Health) or patients affected by Duchenne muscular dystrophy (DMD). **b** Representative confocal Z-stack immunofluorescence images of DMD1 t-NMO stained for desmin (magenta) and TUJ-1 (green). Scale bars, 200 µm. **c** Principal component analysis (PCA) of t-NMO samples from BJ-hiPSCs (black) and DMD1 t-NMOs (red). Each dot represents a single t-NMO. Statistical results are in Supplementary Data 3. **d** Representative whole mount immunofluorescence staining for TUJ-1 (green) and desmin (magenta) of HD1-3, DMD2, DMD3 and DMD4 t-NMOs after 30 days of hiPSC differentiation. Scale bar 200 µm. **e** Scatter dot plot showing the mean area occupied by muscular (desmin$^+$) or neuronal (TUJ-1$^+$) cells in t-NMOs derived from BJ1-3 (black), HD1-3 (scale of green), DMD1 (red), DMD2 (orange), DMD3 (blue) and DMD4 (violet). Data are shown as mean ± s.d. of ≥ 3 independent biological replicates; each dot represent a t-NMO. Each hiPSC line was used for at least one independent t-NMO differentiation experiment. One-way ANOVA with Tukey's multiple comparisons test; n.s., not significant. Statistical results are reported in Supplementary Table 9. **f** Western blot for dystrophy (DYS, upper) and actin (ACT, lower) in BJ1 (black), HD1-3 (scale of green), DMD1 (red), DMD2 (orange), DMD3 (blue) and DMD4 (violet) t-NMOs. As negative control we used dSkM (empty circle). In each lane, proteins extracted from 3 independent biological replicate were loaded. **g** Representative quantification of mean normalized fluorescence intensity variation registered during contraction of t-NMOs stimulated with Glu derived from BJ (black), HD1-3 (scale of green), DMD1 (red), DMD2 (orange), DMD3 (blue) and DMD4 (violet). Data are shown as mean ± s.d. of ≥ 3 independent biological replicates. Each hiPSC line was used for 1 to 3 independent t-NMO differentiation experiments. **h** Violin plot showing the maximum displacement of t-NMOs stimulated with Glu and derived from BJ1-3 (black), HD1-3 (scale of green), DMD1 (red), DMD2 (orange), DMD3 (blue) and DMD4 (violet) using PIVlab. Each violin represents the mean of the displacement vectors obtained from 3 biological replicates per experimental condition (vector number analyzed ≥7580). Each hiPSC line was used for 1 to 3 independent t-NMO differentiation experiments. One-way ANOVA with Tukey's multiple comparisons test showing the statistically significant differences among BJ1-3 and DMD1-4 t-NMOs (*) or HD1-3 and DMD1-4 t-NMOs ($) are reported in Supplementary Table 11. **i** Representative polar charts showing quantification of the maximum displacement (µm) and of the displacement directionality (angle, degree) obtained with PIVlab analysis of t-NMOs stimulated with Glu and derived from BJ1-3 (black), HD1-3 (scale of green), DMD1 (red), DMD2 (orange), DMD3 (blue) and DMD4 (violet). **j** Quantification of calcium peak amplitude ($\Delta F/F_0$) detected with Fluo-4 live imaging analysis upon Glu and ACh stimulation of t-NMOs derived from HD1-3 (scale of green), DMD1 (red), DMD2 (orange), DMD3 (blue) and DMD4 (violet). The fluorescence intensity peak (F) during stimulation was measured and normalized to the baseline fluorescence intensity registered before neurotransmitter stimulation (F0). Data are shown as mean ± s.d. of 3 biological replicates per each condition; each dot represent a t-NMO. Each hiPSC line was used for one independent t-NMO differentiation experiment. One-way ANOVA with Tukey's multiple comparisons test showing the statistically significant differences among HD1-3 and DMD1-4 t-NMOs (*) are reported in Supplementary 12. **k** Upper panels, representative ROIs for Fluo-4 fluorescence imaging analysis of HD t-NMOs and DMD t-NMOs. Scale bar 100 µm. Lower panels, representative Fluo-4 fluorescence intensity variation during time of live imaging acquisition in HD1 t-NMOs and DMD1-4 t-NMOs upon Ach stimulation. Dotted lines correspond to the baseline normalized to 0. Data are shown 3 independent replicates (#) per each sample type, and 3 ROIs (n) for each biological replicate. Each hiPSC line was used for one independent t-NMO differentiation experiment.

support these hypotheses, as we showed that longer, thicker and more oriented myofibers associated with longer and thicker bundles of neuritic projections were identified in t-NMOs (day 30), when compared to time-matched samples derived in absence of dSkM. Of note, the identification of cytoskeleton components of fast and slow myofiber types, and the over-expression of *MYH2* and *MYH8* genes, showed that myofibers could reach a newborn/adult maturation stage in day 30 t-NMOs. Accordingly, contraction and calcium spikes induced by ACh administration were significantly increased in muscular cells derived in presence of dSkMs, when compared to those obtained in absence of dSkM.

Based on this observation we next tested whether t-NMOs possess NMJ and properly respond to a neuromuscular stimulation. After 30 days of hiPSC differentiation, we found that clusters of pre- and post-synaptic elements typical of the NMJs, such as clusters of AChR reached by active axon terminals positive for SV2, were present and promoted by dSkM in t-NMOs. It was previously shown that myofiber innervation and/or muscle fiber maturation promote AChR subunit switch from the embryonic gamma isoform to the adult epsilon isoform[74]. We present data in agreement, as t-NMOs displayed increased expression of the adult epsilon isoform of the *AChR*, when compared to the embryonic gamma isoform. Demonstration of functional integration of the neuromuscular system was confirmed by muscle contraction and calcium flux upon Glu-induced neuronal stimulation, which was abolished upon pre-synaptic and post-synaptic block of NMJs with BoNTA and BTX, respectively[64,65].

Once we had confirmed that dSkMs could be used to generate functional t-NMOs, we investigated whether t-NMOs could be used to model altered functionality of the human skeletal muscle. Toward this aim, we modeled DMD, a well-studied muscle disease caused by mutations in the X-linked dystrophin gene[39], which in vitro has been associated with reduced contraction of muscular cells and altered calcium dynamics[75–77]. We found that t-NMOs derived from four DMD patients showed reduced skeletal muscle contraction, altered calcium transient and flux in the muscular compartment upon neurotransmitter stimulation, when compared to t-NMOs that produce dystrophin (i.e. BJ1-3 and HD1-3 t-NMOs). These phenotypes reproduce key aspects of the disease[78]. Overall, our results demonstrate that patient-specific t-NMOs can be derived by combining hiPSCs and dSkMs and that this platform can be used to investigate and study relevant (dys)functional responses of the human neuromuscular system.

Methods

Human induced pluripotent stem cell derivation and culture

The hiPSC lines used in this study were generated by reprogramming somatic cells in microfluidics[66] (lines: BJ1-3; HD1, DMD1, DMD2, DMD3) or already available (lines: HD2 and HD3[79], and DMD4[80]). For the experiments performed in presence and in absence of dSkM, hiPSCs were generated from human foreskin fibroblast lines (BJ). Three different BJ-derived hiPSC lines were tested (BJ1, BJ2, and BJ3). For DMD1, primary myogenic cells were purchased from Telethon biobank[41]. At the time of primary culture preparation from which hiPSC were derived HD1 was 24-years old, HD2 was 34-years old, HD3 was 43-years old, DMD2 was 15-years old, DMD3 was 14-years old and DMD4 was 10-years old. For these lines informed consent was obtained (ethical committee approval #28062018, University of Milan; #11112021 and #11662022, Policlinico of Milan). DMD carried the following mutations: DMD1, stop codon mutation within the exon 61 (c.9100 C > T) of the *DMD* gene; DMD2, deletion of exons 45–52 in the *DMD* gene; DMD3, deletion of exons 49-52 in the *DMD* gene; DMD4, deletion of exons 45–50 in the *DMD* gene.

Human iPSCs were cultured in feeder free conditions on 0.5% Matrigel Reduced Factor (MRF, Corning) coated cell culture plates (6-multiwell, Sarstedt) in StemMACS iPS-Brew XF (Miltenyi Biotec) at 37 °C in 5% CO_2 in cell incubator. All cell lines were tested negative for mycoplasma and maintained below passage 18 before their use for differentiation.

DSkMs derivation and characterization of mechanical properties

Murine diaphragms were retrieved from 3 to 6-month-old C57BL/6j mice. We have complied with all ethical regulations for animal use (protocol N. 1103/2016 and 418/2020-PR approved by Animal wellness local ethics committee, Organismo per il Benessere Animale OPBA, University of Padova and Fondazione Istituto di Ricerca Pediatrica Città della Speranza and Italian Ministry of Health). After collection, diaphragms were washed 2 times in sterile phosphate buffered saline (PBS, Gibco-Fisher Scientific) and then transferred in deionized water in order to start the decellularization process as previously described[34]. Briefly, diaphragms were processed with 3

detergent-enzymatic treatment (DET) cycles in order to obtain a complete cell removal. Each DET cycle was composed of deionized water at 4 °C for 24 h, 4% sodium deoxycholate (Sigma) at room temperature for 4 h, and 2000 Kunitz DNase-I (Sigma) in 1 M NaCl (Sigma) at RT for 3 h. After decellularization, matrices were washed for at least 3 days in PBS and immediately used or preserved in liquid nitrogen.

For atomic force measurements (AFM), freshly isolated murine diaphragm or dSkM were analyzed by using an Atomic Force Microscope (XEBio), mounted on an Inverted Optical Microscope (Nikon Eclipse Ti). This combination enabled positioning of the AFM tip on the area of interest of the samples. All force-displacement curves were collected using PPP-CONTSCR-10 pyramidal tips mounted on Si3N4 cantilevers with a nominal spring constant of 0.2 N/m (NanoSensors). Cantilever spring constants were calibrated by the manufacturer prior to use. Before each test, the sensitivity of the AFM photodetector was calculated by measuring the slope of force-distance curve acquired on a silicon standard. Indentations were performed at a rate of 0.5 μm/s, producing an indentation with a depth of 2 μm. All AFM measurements were done in a fluid environment (PBS) at room temperature. The Young's modulus was calculated applying a fit of the Hertz model to each individual force curve, assuming a Poisson ratio of 0.5. The moduli of at least 3 samples were calculated as an average over 3–5 sites per sample.

Differentiation of hiPSC toward neuromuscular system

Two days before differentiation (Day −2) hiPSCs were enzymatically dissociated as single cells using TryplE Select (Gibco) and 40,000 cell/cm^2 were seeded onto the specific culture setups. The culture setups used were: 1 cm^2 surgically resected dSkM scaffold for t-NMO derivation, and 0.5% Matrigel reduced factor (MRF, Corning) coated cell culture plates (8-chamberslide, Sarstedt) for the samples derived in absence of dSkM. Upon hiPSC seeding, cells were cultured in StemMACS iPS-Brew XF (Miltenyi Biotec) supplemented with 10 μM StemMACS Y27632 (Miltenyi Biotec) for 24 h (Day-2) and in StemMACS iPS-Brew XF for the following 24 h (Day-1) at 37 °C and 5% CO_2 in cell incubator. The following day (Day0) cells were subjected to the neuromuscular differentiation protocol, that was adapted from literature studies[45]. Briefly, from day 0 to day 2 the media was switched to a Dulbecco's Modified Eagle Medium/Nutrient Mixture F-12 (DMEM F-12, Gibco) basal medium, supplemented with 1X Insulin-Transferrin-Selenium (ITS, Gibco), 1X MEM Nonessential amino-acid solution (MEM NEAA, Gibco), 1% Pen-Strep (Gibco), 3 μM WNT agonist CHIRON99021 (Miltenyi Biotec) and 0.5 μM BMP antagonist LDN193189 (Miltenyi Biotec). From day 3 to day 5, 20 ng/ml fibroblast growth factor-2 (FGF-2, Immunotools) was supplemented to the media used from day 0 to day 2 of differentiation. Starting from day 6, medium was changed to DMEM F-12, supplemented with 15% Knockout™ Serum Replacement (KSR, Gibco), 1X MEM Non-essential amino-acid solution (MEM NEAA, Gibco), 1% Pen-Strep (Gibco), 0.1 mM 2-mercaptoethanol (GIBCO), 10 ng/ml hepatocyte growth factor (HGF, ImmunoTools), 2 ng/ml insulin-like growth factor 1 (IGF-1, Miltenyi Biotec), 20 ng/ml FGF-2 and 0.5 μM LDN193189. From day 8 to day 11 of differentiation cells were cultured in DMEM F-12, supplemented with 15% Knockout™ Serum Replacement (KSR, Gibco), 1X MEM Nonessential amino-acid solution (MEM NEAA, Gibco), 1% Pen-Strep (Gibco), 0.1 mM 2-mercaptoethanol (GIBCO) and 2 ng/ml IGF-1. From day 12, the previous media was modified by including 10 ng/ml HGF and 2 ng/ml IGF-1. From day 26, cells were cultured in myogenic secondary differentiation media composed by DMEM F-12 supplemented with 2% KSR, 1X Insulin-Transferrin-Selenium (ITS, Gibco), 1% Pen-Strep, 1 μM CHIRON99021, 10 ng/ml ciliary neurotrophic factor (CNTF, Peprotech) and 10 ng/ml glial cell line-derived neurotrophic factor (GDNF, Peprotech) until the end point of the experiment. Of note, we did not observe variation in hiPSC seeding among dSkMs derived from different animals.

Immunofluorescence analysis

Samples derived in presence or absence of dSkMs were respectively fixed for 1 h or 10 min in 4% paraformaldehyde (PFA, Sigma-Aldrich) at room temperature. Samples were washed twice in phosphate buffered saline (PBS, Sigma-Aldrich). For t-NMO cryosection staining, samples were embedded in optimum cutting temperature (OCT) compound (Sakura 4583) and sectioned with CM1950 cryostat (Leica). Before starting with the immunostaining, whole mount or cryosections were washed with PBS for 5 min and blocked at room temperature in 1% bovine serum albumin (BSA, Sigma-Aldrich), 0.5% Triton X-100 (Sigma) in PBS (PBST) solution for 2 h. Primary antibodies (Supplementary Table 13) were diluted in 1% BSA PBST solution and incubated for 72 h at 4 °C for whole mount staining, and overnight at 4 °C for cryosections and samples derived in absence of dSkMs. Samples were then washed 3 times for 15 min each in PBST solution and incubated for 48 h (whole mount) at 4 °C and 2 h at room temperature (cryosections and samples derived in absence of dSkMs) with secondary antibodies diluted in blocking solution (Supplementary Table 14). To counterstain the nuclei, 10 μg/mL Hoechst 33342 (ThermoFisher) was supplemented to the secondary antibody solutions. Samples were washed with PBST and mounted with 80% glycerol (Sigma) in PBS. Images were acquired using LSM800 inverted confocal microscope (Zeiss) and Thunder fluorescent stereomicroscope (Leica M205 FCA) equipped with PLANAP0 1.0X objective.

Image preparation and analysis of immunofluorescence images

For contraction and Fluo-4 analysis images were collected using program Analyze of the LASX Leica software of the stereomicroscope Leica M205 FCA. For stereomicroscope imaging we used Leica M205 FCA. For confocal imaging acquisition, the following microscopes were used: confocal Leica TCS SP5 microscope; confocal ZEISS LSM 800 airyscan microscope; Leica Stellaris microscope. We used ImageJ software for adjustments of levels and contrast, maximum and standard deviation intensity projections of the images. All the quantifications reported in the study have been performed considering at least 3 immunofluorescence images for each biological replicate and data were expressed as mean of at least 3 independent biological replicates. Details on the number of replicates used per each specific experiment has been also included in the captions of the figures.

To quantify the number of NANOG$^+$OCT$^+$, TBRA$^-$SOX2$^+$ and TBRA$^+$SOX2$^+$, PAX7$^+$, PAX7$^+$Ki67$^+$ and MYOG$^+$ the Cell Counter tool of ImageJ software (Fiji, v.2.14.0/1.54 f) was used. The number of positive cells for each staining was normalized to the total number of nuclei counted in each field, except for PAX7$^+$Ki67$^+$ cells which were normalized on the total of Pax7$^+$ cells, and expressed as a percentage.

To quantify immunofluorescence area of PAX6$^+$SOX2$^+$ and NEUN$^+$ cells or CHAT$^+$ and MAP2$^+$ neurons, immunofluorescence images were converted in binary masks using the threshold tool and the measurement plugin of ImageJ software (Fiji, v.2.14.0/1.54 f). According to literature[1], the number of positive cells was quantified as a measure of the total cell positive area over the neural area of each sample. For the quantification of MHC$^+$ cells, the area occupied by the MHC$^+$ cells was normalized by the total area of the sample. For neuromuscular compartment quantification, we adopted the same criteria, quantifying the desmin$^+$ and TUJ-1$^+$ area over the total neuromuscular area of the sample.

For the distribution of muscular and neural cells in t-NMO and in samples derived without dSkM, spatial maps were obtained by using 3D surface plot plugin of ImageJ (Fiji) software on immunofluorescence images for desmin/TUJ-1 whole mount-stained samples.

For quantification of directionality and dispersion degree of cells and dSkM myofibers, immunofluorescence images were converted in binary masks using the threshold tool of ImageJ software (Fiji, v.2.14.0/1.54 f) and were analyzed using directionality plugins of ImageJ (Fiji, v.2.14.0/1.54 f). The same criteria was used to quantify myotube and neuritic projection length and thickness of samples stained in whole mount with desmin/myosins and TUJ-1, respectively.

For quantification of the distance of PAX6$^+$SOX2$^+$ and NEUN$^+$ cells from dSkMs, we used command distance of ImageJ software (Fiji, v.2.14.0/1.54 f) to measure the perpendicular distance to the tangent to the dSkM in cross-sections of t-NMO stained for nuclear markers that identified the cell populations. Comparable-sized ROIs were chosen for each of the analyzed images.

For the quantification of NMJ (SV2-BTX co-localization), samples were stained with SV2, BTX, and desmin in whole mount samples. To quantify the number of clusters of BTX co-localized with $SV2^+$ neurites, we used AIVIA AI Image Analysis Software (Aivia Go package version 14.0.0, Leica). Only BTX clusters >2 μm^2 surface area were considered. According to literature[1], the number of SV2-BTX clusters were normalized to the number of myosin$^+$ cells (quantified by using the quantify tool of ImageJ, Fiji, v.2.14.0/1.54 f), present into each corresponding image.

All mentioned ImageJ plugins have source code available and are licensed under open-source GNU GPL v.3 license.

Live imaging analysis

All the analysis in live imaging were performed using Leica M205 FCA stereomicroscope equipped with PLANAP0 1.0X objective, with an acquisition rate of 9 frames per second. When indicated, samples were stimulated with glutamate (Glu) or acetylcholine (ACh) neurotransmitters. Glu solution was prepared using L-Glutamic acid powder (Sigma-Aldrich) dissolved in sterile water to obtain a 100 mM stock solution. ACh (Sigma-Aldrich) was reconstituted in PBS to produce a 100 mM stock solution. Each neurotransmitter solution was administered during live imaging acquisition at the final working concentration of 10 µM. For toxin treatments, samples were incubated with 200 pM Botulinum neurotoxin A (BoNTA) and 1 µg/ml α-bungarotoxin Alexa FluorTM 555 (Invitrogen, B13422) for 12 h at 37 °C, before live imaging acquisition and analysis. BoNTA was kindly provided by Prof. Cesare Montecucco, University of Padua, IT.

For contraction analysis, samples were monitored during time of imaging acquisition using bright field imaging or fluorescence imaging after treatment with calcein staining (LifeTechnologies). Briefly, for calcein staining samples were washed with PBS and subsequently incubated with a working solution of 3 µM calcein in serum-free cell medium for 30 min at 37 °C and 5% CO_2, and further washed with PBS before imaging. Variation of pixel intensities during the time of imaging acquisition were measured considering whole mount samples or, where indicated, for specific ROI accurately selected in correspondence with myogenic area (sized >100 μm^2) using the Quantify tool of the Leica Application Suite X (LAS X) software. We also confirmed that the same quantifications were obtained by providing lif files from LAS X to Image J plugin Spiky[81] (Supplementary Fig. 2h). Briefly, Spiky performs a detection of pixel intensity variation during the time of imaging recording. For our experiments we used a minimum peak amplitude equal to 8% and a start peak threshold equal to 2% for detection. These values were empirically found to fit for all the samples analyzed, when compared with LAS X Leica software. Independently from the LASX- or Spiky-derived.csv files used, we implemented MATLAB 2021 software (MathWorks) to remove neurotransmitter administration-based artifacts and photobleaching. Toward this aim, when neurotransmitters are supplemented to the samples, a MATLAB 2021 algorithm was designed to resolve signal artifacts given to media perturbation, that applied the Modified Akima piecewise cubic Hermite interpolation technique, present by default in MATLAB with makima function, that uses a cubic interpolation to produce piecewise polynomials with continuous first order derivative[82,83]. For all the samples analyzed, photobleaching was resolved by implementing a fitting correction with a double exponential decay model by using a MATLAB 2021 code, in particular the fit function present in the curve fitting toolbox. Additionally, applying the "normalize" option of the fit function, intensity variation datasets were normalized to compare different samples.

For calcium experiments, samples were treated with Fluo-4-AM (Invitrogen F14201) at day 30 of differentiation following the protocol instruction. Briefly, after PBS wash, samples were incubated with 20 µM Fluo-4-AM (Invitrogen), 5 µl/ml Pluronic^{TM} F-127 (Thermo Fisher Scientific), and 12.5 µl/ml sulfinpyrazone (Sigma-Aldrich) in serum-free cell medium for 30 min at 37 °C and 5% CO_2. Samples were then accurately washed with myogenic secondary differentiation media without KSR and subjected to live imaging analysis. Live imaging was performed as previously described in whole mount samples. For calcium transient analysis, ≥6 ROIs per sample with a size of 20 μm^2 were selected to evaluate the mean fluorescence intensity variation of restricted group of myofibers identified for their morphology. ROI fluorescence intensity variations were analyzed using the tool Process of the LAS X Leica software or ImageJ plugin Spiky. Obtained data were processed and normalized with the same MATLAB code described for contraction to express calcium variation during the time of imaging acquisition. For calcium $\Delta F/F_0$ calculation, the same selected ROIs used for calcium flux analysis were employed to identify baseline (before neurotransmitter stimulation, F_0) and maximum (after neurotransmitter stimulation, F_{peak}) fluorescence intensity values. Measure plugin of ImageJ was used to quantify the $\Delta F/F_0$ on arbitrarily extracted lif frames from LAS X Laica software. The same results can be also reproduced by applying *max* and *mean* functions of MATLAB on outputted ImageJ plugin Spiky or LAS X csv files. $\Delta F/F_0$ was calculated considering ΔF as F_{peak} - F_0, with F_{peak} as maximum fluorescence intensity measured upon neurotransmitter stimulation and F_0 as baseline.

For vector map generation and displacement measurements, a graphical user interface (GUI) based particle image velocimetry software (PIVlab) version 3.07 was used according to literature[51–54]. Briefly, selected pairs of frames acquired during live imaging analysis were cross-correlated to yield vectorial maps and local displacement. In particular, for the quantification of the spontaneous contraction, we analyzed frames before contraction to reveal t-NMOs relaxation and frames before and after contraction for the maximum displacement; maximum displacement was quantified by cross-correlating pairs of frames acquired before contraction and at the maximum displacement of t-NMOs. Quantification of the displacement and direction of vectors was obtained using Multipass Fast Fourier Transform (FFT) window deformation PIV algorithm and stored as correlation matrix in a mat file. Polar charts showing the relation between displacement and direction of vectors for each sample were built from a custom-made R (v. 4.3.1) script using package ggplot2 v. 3.5.1[84].

All mentioned MATLAB algorithms have source code available in MATLAB documentation, GraphPad Prism v.10, ImageJ plugins licensed under open-source GNU GPL v.3 license.

RNA purification and RT-qPCR

Total cell RNA was isolated and purified using RNeasy Plus Mini Kit (Qiagen) according to the manufacturer's instructions. Briefly, cells differentiated without dSkM were harvested by direct lysis in the cell culture well. t-NMO samples were accurately disrupted and homogenized with sterile scissors prior to extraction. All the harvested and homogenized samples were lysed with RNeasy Plus lysis buffer (RLT, Qiagen) and further processed according to the protocol. Extracted RNA quality and concentration were assessed with Nanodrop (Thermo Scientific). Complementary DNA (cDNA) of t-NMO and cells differentiated without dSkM was obtained using High Capacity cDNA Reverse Transcription Kit (Applied Biosystems,) in a dedicated thermocycler (Mastercycler X50a, Eppendorf).

Expression of myogenic and neural markers was quantified by using a 7500 Fast Real-Time PCR System (Applied Biosystem) and Platinum SYBR Green SuperMix kit components (Invitrogen, 11733-038) according to the manufacturer's instructions. All the primers used are listed in Supplementary Table 15.

Target Ct values of gene expression were normalized to that of the housekeeping genes GAPDH or myosin heavy chain. Data are shown as relative fold change of gene expression in respect to the samples obtained in absence of dSkM condition applying the $2^{-\Delta\Delta CT}$ method, and hiPSCs were used as negative control.

Bulk RNA-sequencing analysis

Total RNA was quantified using the Qubit 4.0 fluorometric Assay (Thermo Fisher Scientific). Libraries were prepared from 125 ng of total RNA using the NEGEDIA Digital mRNA-seq research grade sequencing service (Negedia srl)[85] which included library preparation, quality assessment and sequencing on a NovaSeq 6000 sequencing system using a single-end, 100 cycle strategy (Illumina Inc.).

The raw data were analyzed by Negedia srl proprietary NEGEDIA Digital mRNA-seq pipeline (v2.0) which involves a cleaning step by quality filtering and trimming, alignment to the reference genome and counting by gene[86,87].

Bioinformatic analysis was performed in R v. 4.2. Genes were annotated using R package org.Hs.eg.db v. 3.16. Genes were filtered out if not having more than half replicates from the same culture condition with at least 2 raw counts. Raw counts were subsequently normalized and expressed as counts per million (CPM) using R package DESeq2 v. 1.38[88]. Log2 scale CPM data were obtained by adding a unit pseudo-count to avoid infinite values. PCA was performed by R stats package function *prcomp* by singular value decomposition (SVD) after centering. Differentially expressed genes (DEGs) were computed using DESeq2 starting from raw count data, using a *P* value, after correction by the Benjamini-Hochberg method, lower than 0.01. DEGs between t-NMO and samples derived in absence of dSkM condition were input for an over-representation analysis within Gene Ontology (GO, https://www.ebi.ac.uk/GOA) and Reactome (https://reactome.org/) databases. The analysis was performed using ClueGO v. 2. 5[89]. within Cytoscape v. 3.10[90]. environment for network visualization. A Benjamini-Hochberg corrected *P* value cutoff of 0.001 was set. Hierarchical clustering with heat map visualization was performed using R package pheatmap v. 1.0.12, using Euclidean distance.

Western blotting

For protein extraction, 3 dSkM and 3 frozen t-NMOs (day30) derived from BJ1, HD1-3 and DMD1-4 were mechanically pulverized in liquid nitrogen vapors using a motor pestle (Kimble), and homogenized in a lysis buffer (50 mM Tris HCL; pH 7.5, 150 mM NaCl; 1 mM EDTA; 10% glycerol; 0.5 mM DTT; 2% SDS; 1% Triton X-100) containing protease and phosphatase inhibitors (Complete EDTA free, Roche; Cocktail II and III, Sigma). Proteins were quantified using the BCA Protein Assay kit (Pierce, Thermo Fisher).

Protein extracts (30 µg) were loaded onto an 8% SDS-PAGE gel prepared according to standard protocols and electrophoresed at 80 V through the stacking gel and 120 V through the separating gel. Proteins were transferred to a nitrocellulose membrane using the Bio-Rad Trans-Blot Turbo System (2.5 A, 25 V, 10 min) in a methanol-based transfer buffer. Transfer efficiency was confirmed with Coomassie blue staining. After Red Ponceau staining (Sigma-Aldrich), membranes were blocked with Every-Blot Blocking Buffer (Bio-Rad) and incubated overnight at 4 °C with mouse monoclonal anti-dystrophin antibody (NCL-DYS2, Novocastra, diluted 1:50). After three washes with TBS-T, membranes were incubated with HRP-conjugated secondary antibodies (Dako, 1:1000) for 90 min. Chemiluminescent detection was performed using Immobilon Western HRP substrate (Millipore). Signals were visualized using the Bio-Rad ChemiDoc imaging system and quantified with ImageLab software.

Statistics and reproducibility

All analyses were performed with GraphPad prism 6. We expressed data as mean ± s.d of multiple biological replicates (as indicated in the figure legend). We determined statistical significance by unequal variance Student's t-test, one-way analysis of variance (ANOVA) and Tukey's multiple comparison test. When needed, statistical significance is shown in Supplementary Tables 1–12. A *P* value of less than 0.05 was considered statistically significant.

Reporting summary

Further information on research design is available in the Nature Portfolio Reporting Summary linked to this article.

Data availability

Bulk RNA-seq data are available at NCBI Gene Expression Omnibus (GEO) database within the series GSE226477 (samples GSM7076294-GSM7076296, GSM7076300-GSM7076302, and GSM7076303-GSM7076308). Bioinformatic analysis has been performed with publicly available tools according to developers' instructions. The source data for the main and Supplementary Figs. are available as Supplementary Data 1–4, and all other data are available from the corresponding author on reasonable request.

Code availability

All scripts and custom code are available upon request to the corresponding author.

Received: 5 July 2024; Accepted: 4 July 2025;
Published online: 19 July 2025

References

1. Urzi, A. et al. Efficient generation of a self-organizing neuromuscular junction model from human pluripotent stem cells. *Nat. Commun*. **14**, 1–15 (2023).
2. Fralish, Z., Lotz, E. M., Chavez, T., Khodabukus, A. & Bursac, N. Neuromuscular development and disease: Learning from in vitro and in vivo Models. *Front. Cell Dev. Biol.* **9**, 1–35 (2021).
3. Faustino Martins, J. M. et al. Self-organizing 3D human trunk neuromuscular organoids. *Cell Stem Cell* **26**, 172–186.e6 (2020).
4. Zhang, K., Bai, L., Xu, W. & Shen, C. Human neuromuscular junction three-dimensional organoid models and the insight in motor disorders. *J. Mol. Cell Biol.* **13**, 767–773 (2021).
5. Pereira, J. D. et al. Human sensorimotor organoids derived from healthy and amyotrophic lateral sclerosis stem cells form neuromuscular junctions. *Nat. Commun*. **12**, 1–17 (2021).
6. Moyle, L. A., Jacques, E. & Gilbert, P. M. Engineering the next generation of human skeletal muscle models: From cellular complexity to disease modeling. *Curr. Opin. Biomed. Eng.* **16**, 9–18 at https://doi.org/10.1016/j.cobme.2020.05.006 (2020).
7. Gao, C. et al. Neuromuscular organoids model spinal neuromuscular pathologies in C9orf72 amyotrophic lateral sclerosis. *CellReports* **43**, 113892 (2024).
8. Shin, M. K. et al. Generation of skeletal muscle organoids from human pluripotent stem cells to model myogenesis and muscle regeneration. *Int. J. Mol. Sci*. **23**, 1–14 (2022).
9. Slater, C. R. The structure of human neuromuscular junctions: Some unanswered molecular questions. *Int. J. Mol. Sci.* 18 at https://doi.org/10.3390/ijms18102183 (2017).
10. Jones, R. A. et al. Cellular and molecular anatomy of the human neuromuscular junction. *Cell Rep.* **21**, 2348–2356 (2017).
11. Wu, H., Xiong, W. C. & Mei, L. To build a synapse: Signaling pathways in neuromuscular junction assembly. *Development* at https://doi.org/10.1242/dev.038711 (2010).
12. Tani, S., Chung, U. il, Ohba, S. & Hojo, H. Understanding paraxial mesoderm development and sclerotome specification for skeletal repair. *Exp. Mol. Med.* **52**, 1166–1177 (2020).
13. Chal, J. & Pourquié, O. Making muscle: Skeletal myogenesis in vivo and in vitro. *Development (Cambridge)* 144 2104–2122 at https://doi.org/10.1242/dev.151035 (2017).
14. Li, L., Xiong, W.-C. & Mei, L. Neuromuscular junction formation, aging, and disorders. *Annu. Rev. Physiol.* https://doi.org/10.1146/annurev-physiol-022516 (2018).
15. Bonnans, C., Chou, J. & Werb, Z. Remodelling the extracellular matrix in development and disease. *Nat. Rev. Mol. Cell Biol.* **15**, 786–801 (2014).
16. Rozario, T. & DeSimone, D. W. The extracellular matrix in development and morphogenesis: A dynamic view. *Dev. Biol.* **341**, 126–140 (2010).
17. Csapo, R., Gumpenberger, M. & Wessner, B. Skeletal muscle extracellular matrix – what do we know about its composition, regulation, and physiological roles? a narrative review. *Front. Physiol.* 11 at https://doi.org/10.3389/fphys.2020.00253 (2020).
18. Zhang, W., Liu, Y. & Zhang, H. Extracellular matrix: An important regulator of cell functions and skeletal muscle development. *Cell Biosci.* **11**, 1–13 (2021).

19. Myers, J. P., Santiago-medina, M. & Gomez, T. M. Regulation of axonal outgrowth and pathfinding by integrin-ECM interactions. *Dev. Neurobiol.* **71**, 901–923 (2012).
20. Roberts, T. J. et al. The multi-scale, three-dimensional nature of skeletal muscle contraction. *Physiology* **34**, 402–408 (2019).
21. Urciuolo, A. et al. Collagen VI regulates satellite cell self-renewal and muscle regeneration. *Nat. Commun*. **4**, 1–13 (2013).
22. Gattazzo, F., Urciuolo, A. & Bonaldo, P. Extracellular matrix: A dynamic microenvironment for stem cell niche. *Biochimica et Biophysica Acta - General Subjects* at https://doi.org/10.1016/j.bbagen.2014.01.010 (2014).
23. Schüler, S. C. et al. Extracellular matrix: Brick and mortar in the skeletal muscle stem cell niche. *Front. Cell Dev. Biol.* **10**, 1–21 (2022).
24. Barros, C. S., Franco, S. J. & Müller, U. Extracellular Matrix: Functions in the nervous system. *Cold Spring Harb. Perspect. Biol.* **3**, 1–24 (2011).
25. Melrose, J., Hayes, A. J. & Bix, G. The CNS/PNS extracellular matrix provides instructive guidance cues to neural cells and neuroregulatory proteins in neural development and repair. *Int. J. Mol. Sci*. **22**, 1–35 (2021).
26. Chen, P., Cescon, M. & Bonaldo, P. The role of collagens in peripheral nerve myelination and function. *Mol. Neurobiol.* **52**, 216–225 (2015).
27. Cescon, M. et al. Collagen VI is required for the structural and functional integrity of the neuromuscular junction. *Acta Neuropathol.* **136**, 483–499 (2018).
28. Singhal, N. & Martin, P. T. Role of extracellular matrix proteins and their receptors in the development of the vertebrate neuromuscular junction. *Dev. Neurobiol.* **71**, 982–1005 (2011).
29. Urciuolo, A. et al. Decellularised skeletal muscles allow functional muscle regeneration by promoting host cell migration. *Sci. Rep.* **8**, 8398 (2018).
30. Urciuolo, A. & De Coppi, P. Decellularized tissue for muscle regeneration. *Int. J. Mol. Sci.* 19 at https://doi.org/10.3390/ijms19082392 (2018).
31. Trevisan, C. et al. Generation of a functioning and self-renewing diaphragmatic muscle construct. *Stem Cells Transl. Med.* **8**, 858–869 (2019).
32. Trevisan, C. et al. Allogenic tissue-specific decellularized scaffolds promote long-term muscle innervation and functional recovery in a surgical diaphragmatic hernia model. *Acta Biomater.* **89**, 115–125 (2019).
33. Raffa, P. et al. Decellularized skeletal muscles support the generation of in vitro neuromuscular tissue models. *Appl. Sci.* **11**, 1233–1243 (2021).
34. Piccoli, M., Trevisan, C., Maghin, E., Franzin, C. & Pozzobon, M. Mouse skeletal muscle decellularization. in *Methods in Molecular Biology* vol. 1577 87–93 (Humana Press Inc., 2018).
35. Maghin, E. et al. Customized bioreactor enables the production of 3D diaphragmatic constructs influencing matrix remodeling and fibroblast overgrowth. *npj Regen. Med.* **7**, 25 (2022).
36. Quarta, M. et al. Bioengineered constructs combined with exercise enhance stem cell-mediated treatment of volumetric muscle loss. https://doi.org/10.1038/ncomms15613 (2017).
37. Piccoli, M. et al. Improvement of diaphragmatic performance through orthotopic application of decellularized extracellular matrix patch. *Biomaterials* **74**, 245–255 (2016).
38. Raffa, P. et al. Decellularized skeletal muscles display neurotrophic effects in three-dimensional organotypic cultures. https://doi.org/10.1002/sctm.20-0090 (2020).
39. Duan, D., Goemans, N., Takeda, S., Mercuri, E. & Aartsma-Rus, A. Duchenne muscular dystrophy. *Nat. Rev. Dis. Primers* 7 at https://doi.org/10.1038/s41572-021-00248-3 (2021).
40. Lovering, R. M., Iyer, S. R., Edwards, B. & Davies, K. E. Alterations of neuromuscular junctions in Duchenne muscular dystrophy. *Neurosci. Lett.* 737 at https://doi.org/10.1016/j.neulet.2020.135304 (2020).
41. Lim, K. R. Q., Nguyen, Q. & Yokota, T. Genotype-phenotype correlations in duchenne and becker muscular dystrophy patients from the canadian neuromuscular disease registry. *J. Pers. Med.* **10**, 1–18 (2020).
42. Belhasan, D. C. & Akaaboune, M. The role of the dystrophin glycoprotein complex on the neuromuscular system. *Neurosci. Lett.* 722 at https://doi.org/10.1016/j.neulet.2020.134833 (2020).
43. Stuelsatz, P., Keire, P., Almuly, R. & Yablonka-Reuveni, Z. A contemporary atlas of the mouse diaphragm: Myogenicity, vascularity, and the Pax3 connection. *J. Histochem. Cytochem.* **60**, 638–657 (2012).
44. Sefton, E. M., Gallardo, M. & Kardon, G. Developmental origin and morphogenesis of the diaphragm, an essential mammalian muscle. *Dev. Biol.* **440**, 64–73 (2018).
45. Chal, J. et al. Generation of human muscle fibers and satellite-like cells from human pluripotent stem cells in vitro. *Nat. Protoc.* **11**, 1833–1850 (2016).
46. Rossi, L. et al. Engineering assembloids to mimic graft-host skeletal muscle interaction. *Adv. Healthc. Mater.* **2404111**, 1–17 (2025).
47. Xi, H. et al. A human skeletal muscle atlas identifies the trajectories of stem and progenitor cells across development and from human pluripotent stem cells. *Cell Stem Cell* **27**, 158–176.e10 (2020).
48. Gouti, M. et al. A gene regulatory network balances neural and mesoderm specification during vertebrate trunk development. *Dev. Cell* **41**, 243–261.e7 (2017).
49. Sambasivan, R. & Steventon, B. Neuromesodermal progenitors: A basis for robust axial patterning in development and evolution. *Front. Cell Dev. Biol.* **8**, 1–9 (2021).
50. Sagner, A. & Briscoe, J. Morphogen interpretation: Concentration, time, competence, and signaling dynamics. *Wiley Interdiscip. Rev. Dev. Biol.* **6**, 1–19 (2017).
51. Villeneuve, C. et al. Mechanical forces across compartments coordinate cell shape and fate transitions to generate tissue architecture. *Nat. Cell Biol.* **26**, 207–218 (2024).
52. Shim, G., Breinyn, I. B., Martínez-Calvo, A., Rao, S. & Cohen, D. J. Bioelectric stimulation controls tissue shape and size. *Nat. Commun.* **15**, 2938 (2024).
53. Thielicke, W. & Sonntag, R. Particle image velocimetry for MATLAB: Accuracy and enhanced algorithms in PIVlab. *J. Open Res. Softw.* **9**, 1–14 (2021).
54. Cheesbrough, A. et al. A scalable human iPSC-based neuromuscular disease model on suspended biobased elastomer nanofiber scaffolds. *Biofabrication* **15**, 45020 (2023).
55. Grespan, E. et al. Analysis of calcium transients and uniaxial contraction force in single human embryonic stem cell-derived cardiomyocytes on microstructured elastic substrate with spatially controlled surface chemistries. *Langmuir* **32**, 12190–12201 (2016).
56. Schiaffino, S., Rossi, A. C., Smerdu, V., Leinwand, L. A. & Reggiani, C. Developmental myosins: Expression patterns and functional significance. *Skelet. Muscle* **5**, 1–14 (2015).
57. Mackey, A. L., Magnan, M., Chazaud, B. & Kjaer, M. Human skeletal muscle fibroblasts stimulate in vitro myogenesis and in vivo muscle regeneration. *J. Physiol.* **595**, 5115–5127 (2017).
58. Thakurela, S. et al. Mapping gene regulatory circuitry of Pax6 during neurogenesis. *Cell Discov.* **2**, 15045 (2016).
59. Gusel'nikova, V. V. & Korzhevskiy, D. E. NeuN as a neuronal nuclear antigen and neuron differentiation marker. *Acta Nat.* **7**, 42–47 (2015).
60. Qu, Q. et al. High-efficiency motor neuron differentiation from human pluripotent stem cells and the function of Islet-1. *Nat. Commun*. **5**, 1–13 (2014).
61. Liu, Z. et al. Specific marker expression and cell state of Schwann cells during culture in vitro. *PLoS One* **10**, 1–17 (2015).
62. Cetin, H., Beeson, D., Vincent, A. & Webster, R. The structure, function, and physiology of the fetal and adult acetylcholine receptor in muscle. *Front. Mol. Neurosci.* **13**, 1–14 (2020).

63. Missias, A. C., Chu, G. C., Klocke, B. J., Sanes, J. R. & Merlie, J. P. Maturation of the acetylcholine receptor in skeletal muscle: Regulation of the AChR γ-to-ε switch. *Dev. Biol.* **179**, 223–238 (1996).
64. Dressler, D. & Saberi, F. A. Botulinum toxin: Mechanisms of action. *Eur. Neurol.* 53 at https://doi.org/10.1159/000083259 (2005).
65. Miledi, R., Molenaar, P. C. & Polak, R. L. α-Bungarotoxin enhances transmitter 'released' at the neuromuscular junction. *Nature* **272**, 641–643 (1978).
66. Gagliano, O. et al. Microfluidic reprogramming to pluripotency of human somatic cells. *Nat. Protoc.* **14**, 722–737 (2019).
67. Hofer, M. & Lutolf, M. P. Engineering organoids. *Nat. Rev. Mater.* **6**, 402–420 (2021).
68. Zhao, Z. et al. Organoids. *Nat. Rev. Methods Prim.* **2**, 1–21 (2022).
69. Thorsteinsdottir, S., Deries, M., Cachaço, A. S. & Bajanca, F. The extracellular matrix dimension of skeletal muscle development. *Dev. Biol.* **354**, 191–207 (2011).
70. Shahin-shamsabadi, A. & Cappuccitti, J. In vivo-like scaffold-free 3D in vitro models of muscular dystrophies. *Case Anchored Cell Sheet Eng. Personalized Med.* **2404465**, 1–16 (2024).
71. Shahriyari, M. et al. Protocol to develop force-generating human skeletal muscle organoids. *STAR Protoc.* **5**, 102794 (2024).
72. Osaki, T., Uzel, S. G. M. & Kamm, R. D. On-chip 3D neuromuscular model for drug screening and precision medicine in neuromuscular disease. *Nat. Protoc.* **15**, 421–449 (2020).
73. Gallo, G. & Letourneau, P. C. Localized sources of neurotrophins initiate axon collateral sprouting. *J. Neurosci.* **18**, 5403–5414 (1998).
74. Bakooshli, M. A. et al. A three-dimensional culture model of innervated human skeletal muscle enables studies of the adult neuromuscular junction and disease modeling. *bioRxiv* 1–29 (2018).
75. Tejedera-Villafranca, A., Montolio, M., Ramón-Azcón, J. & Fernández-Costa, J. M. Mimicking sarcolemmal damage in vitro: A contractile 3D model of skeletal muscle for drug testing in Duchenne muscular dystrophy. *Biofabrication* **15**, 1–16 (2023).
76. Nesmith, A. P. et al. A human in vitro model of Duchenne muscular dystrophy muscle formation and contractility. *J. Cell Biol.* **215**, 47–56 (2016).
77. Al Tanoury, Z. et al. Prednisolone rescues Duchenne muscular dystrophy phenotypes in human pluripotent stem cell-derived skeletal muscle in vitro. *Proc. Natl. Acad. Sci. USA* **118**, 1–12 (2021).
78. Ebrahimi, M. et al. De novo revertant fiber formation and therapy testing in a 3D culture model of Duchenne muscular dystrophy skeletal muscle. *Acta Biomater.* **132**, 227–244 (2021).
79. Monzio Compagnoni, G. et al. Mitochondrial dysfunction in fibroblasts of Multiple System Atrophy. *Biochim. Biophys. Acta - Mol. Basis Dis.* **1864**, 3588–3597 (2018).
80. Rovina, D. et al. Reprogramming of dermal fibroblasts from a Duchenne muscular dystrophy patient carrying a deletion of exons 45–50 into an induced pluripotent stem cell line (CCMi005-A). *Stem Cell Res*. **64**, 102889 (2022).
81. Pasqualin, C. et al. Spiky: An ImageJ Plugin for Data Analysis of Functional Cardiac and Cardiomyocyte Studies. *J. Imaging* **8**, 95 (2022).
82. Akima, H. A New Method of Interpolation and Smooth Curve Fitting Based on Local Procedures. *J. ACM* **17**, 589–602 (1970).
83. Akima, H. A Method of Bivariate Interpolation and Smooth Surface Fitting Based on Local Procedures. *Commun. ACM* **17**, 18–20 (1974).
84. H, W. ggplot2: Elegant Graphics for Data Analysis. *Springer-Verlag New York* **ISBN 978-3**, (2016).
85. Xiong, Y. et al. A Comparison of mRNA Sequencing with Random Primed and 3′-Directed Libraries. *Sci. Rep*. **7**, 1–12 (2017).
86. Anders, S., Pyl, P. T. & Huber, W. HTSeq-A Python framework to work with high-throughput sequencing data. *Bioinformatics* **31**, 166–169 (2015).
87. Dobin, A. et al. STAR: Ultrafast universal RNA-seq aligner. *Bioinformatics* **29**, 15–21 (2013).
88. Love, M. I., Huber, W. & Anders, S. Moderated estimation of fold change and dispersion for RNA-seq data with DESeq2. 1–21 https://doi.org/10.1186/s13059-014-0550-8 (2014).
89. Bindea, G. et al. ClueGO: a Cytoscape plug-in to decipher functionally grouped gene ontology and. *Pathw. Annotation Netw.* **25**, 1091–1093 (2009).
90. Paul Shannon, 1 et al. Cytoscape: A software environment for integrated models. *Genome Res*. **13**, 426 (1971).

Acknowledgements

This work was supported by STARS Starting Grant 2017 of University of Padova (grant code LS3-19613), by Bando Direzione Scientifica IRP Città della Speranza (grant code 21/05), by BIRD (code BIRD2223_01), and by AIRC under MFAG (code 29118) supported by Panciera Foundation to A.U.; by AFM Telethon (grant code) to N.E.; and by Bando CARIPARO-Ricerca Pediatrica 2020-2022 (grant number 20/17 FCR) to M.P. O.G. was supported by University of Padova under the 2019 STARS Grants program (iNeurons). MC is funded by Italian Ministry of University and Research and European Union (Next Generation EU - MUR-PRIN 2022-PNRR: project P2022Y2A3L, CUP C53D23007520001; project 20227YB93W, CUP C53D23003030001), by the European Union (Next Generation EU, Project CN00000041, CUP B93D21010860004, Spoke n. 5 "Inflammatory and infectious diseases") and by Telethon-AFM (#28703). DC is funded by Fondazione Telethon Core Grant, Armenise-Harvard Foundation Career Development Award. DC Is funded by Italian Ministry of Health (Piano Operativo Salute Traiettoria 3, T3-AN-09, "Genomed"; Ricerca Finalizzata 2021, "genOMICA"; MCNT2 2023, "EUCARDIS"), Italian Ministry of University and Research and European Union (Next Generation EU - MUR-PRIN-2022 CUP 2022T7XP29, Project PNC 0000001 D3-4-Health). YT and CV were supported by "Multiomics pRofiling of patient spEcific Models to predict druggable targets in severe neuromuscular rare diseases (REMODEL)", Unmet Medical Needs, Fondazione Regionale per la Ricerca Biomedica (FRRB, 2022), and Piano Nazionale di Ripresa e Resilienza (PNRR), Next Generation EU and MUR (National Center for Gene Therapy and Drugs based on RNA Technology, Spoke #1: Genetic diseases, PNRR CN3 RNA, 2022). DMD1 cell lines were provided by the Bank of muscle tissue, peripheral nerve, DNA and Cell Culture, member of Telethon network of Genetic biobanks, at Fondazione IRCCS Ca' Granda, Ospedale Maggiore Policlinico, Milano, Italy. We thank Marco Braggion and Marco La Placa for helping with MATLAB software. Schematic illustrations in Fig. 1a (license OA28DQLURL), 4 f (license n. FB28DQM7K2), 5a (license n. ZX28DQMK2W), Supplementary Figs. 1 g and 3a (license n. NA28DQMW6L) and the Graphical Abstract (license n. UH28DQKW6L) were created with BioRender.com.

Author contributions

A.U. designed the study. B.A. performed the differentiation experiments and analysis. F.C, L.R., G.B., P.C., A.L., contributed to sample preparation and imaging analysis. A.U., B.A., P.C., L.R, F.C., G.C., and A.L. performed the live imaging analysis. P.R. and M.E. helped in setting the seeding strategies. O.G., S.A., and W.Q performed cell reprogramming. C.La. contributed to neural characterization and data interpretation. E.M. and M.P. derived dSkM. M.G. performed AFM analysis and data interpretation. D.C. performed RNA-sequencing. M.C. and S.C. contributed to NMJ imaging analysis and protein extraction. R.F. contributed in the generation of DMD3 hiPSCs by microfluidic reprogramming. C.Lu. analyzed RNA-sequencing data and interpretation. L.S. contributed in RNA-sequencing analysis and in the quantification of t-NMO contraction with PIVlab, and in the graphical representation. C.V. and Y.T. provided DMD2, DMD3, HD1 primary cells and HD2, HD3 and DMD4 hiPSCs and performed the western blot analysis and data interpretation. N.E. supervised the reprogramming and critically contributed to the transcriptomic

analysis and to data interpretation. All the authors contributed to the revision of the manuscript. A.U. analyzed and interpreted the data, wrote the manuscript and supervised the project.

Competing interests
The authors declare no competing interests.

Additional information
Supplementary information The online version contains supplementary material available at https://doi.org/10.1038/s42003-025-08484-z.

Correspondence and requests for materials should be addressed to Anna Urciuolo.

Peer review information *Communications Biology* thanks the anonymous reviewers for their contribution to the peer review of this work. Primary handling editors: Ken-ichiro Kamei and Ophelia Bu.